Spring 2024

Large Sample Statistical Study of Three-Dimensional Magnetic Reconnection at the Swarthmore Spheromak Experiment

Solomon Murdock , '24

Large Sample Statistical Study of Three-Dimensional Magnetic Reconnection at the Swarthmore Spheromak Experiment

Solomon Murdock

2 June 2024

Abstract

Many plasmas can be described by ideal magnetohydrodynamics (MHD). A key result of ideal MHD is the frozen-in-flux theorem which states that the magnetic field stretches and bends with the motion of the plasma. The frozen-in-flux theorem is violated during magnetic reconnection, the annihilation of magnetic flux within a plasma. During reconnection, non-ideal MHD effects dominate plasma dynamics. The dynamics of magnetic reconnection is an unsolved problem in plasma physics. Most prior laboratory studies of magnetic reconnection examined reconnection in 2D scenarios, scenarios with a single ignorable coordinate. The SSX device was used to merge twisted ropes of plasma called Taylor states which undergo 3D magnetic reconnection, reconnection without an ignorable coordinate, as they collide. The merging occurs in an unconfined volume at the center of SSX. The experiment measured the line averaged electron density and ion temperature along two different chords in the SSX midplane and measured the magnetic field on a grid of 16 coplanar positions in the merging region. We recorded data on 604 instances of Taylor state merging. The merging of Taylor states involves oscillations in density, magnetic energy, and ion temperature. Each quantity attains multiple significant peaks during each shot. The geometry of the current density in the merging region varies over the course of each shot. We calculated 11 summary statistics for each shot including the average and peak density, ion temperature, and magnetic energy and report their distributions. Neither average or peak magnetic energy is correlated with average or peak ion temperature despite ion heating being a known consequence of magnetic reconnection. The merging of Taylor states is much more complex and dynamic than two-dimensional magnetic reconnection.

1 Introduction

1.1 Plasma

A plasma is an ionized gas, a gas that contains negative electrons and positive ions. Plasma is rarely observed on earth, because free electrons and positive ions attract each other and spontaneously combine to form atoms or molecules depending on the nature of ions. However, at high temperatures, electrons have enough energy to remain detached from their respective ions. Familiar examples of plasma include the matter that makes up stars, the interstellar medium, and lightning. Plasma can also be created in the laboratory by heating an ordinary gas to high temperatures.

The charges in a plasma can move to generate currents within the plasma. These currents create a magnetic field just like currents in wires. The magnetic field created by the currents in the plasma exerts a force on the currents. When the magnetic field exerts a strong enough force on the plasma to significantly affect its behavior, we call the plasma a magnetized plasma. What is considered significant depends on the precision of the measurements being made on the plasma. If the magnetic field is necessary to describe the observed plasma dynamics, the plasma is considered magnetized. There is a complex interplay between the current and magnetic field in a magnetized plasma, because two processes are simultaneously at play. The current geometry determines the magnetic field, and at the same time, the magnetic field exerts forces on the plasma driving the currents.

1.2 The Problem of Magnetic Reconnection

There are three main models of a plasma, the Vlasov model, the two-fluid model, and magnetohydrodynamics. Magnetohydrodynamics, MHD, is actually a family of very closely related theories rather than a single theory. It includes many variants, such as resistive MHD and ideal MHD, which will be detailed later in this thesis. The simplest model of a plasma, ideal MHD, is a special case of the two-fluid model which itself is a special case of the Vlasov model. Upon making certain assumptions, the two-fluid equations can be simplified to the ideal MHD equations. Ideal MHD is able to describe most of the dynamics of many plasmas including the solar corona, the interstellar medium, and the plasma inside a tokamak, a potential configuration for a nuclear fusion reactor. However, these plasmas do display some deviation from ideal MHD.

Within the framework of ideal magnetohydrodynamics, one can prove Alfv́en's theorem which is also known as the frozen-in-flux theorem. This theorem, which will be proved later in this thesis, states that the magnetic flux through any closed surface which moves along the velocity field of the plasma is constant. As the particles that make up the plasma move, the magnetic field lines stretch and bend as if they are attached to the fluid. When the frozen-in-flux theorem holds, the magnetic field in a plasma can be thought of as being frozen into the plasma.

Ideal MHD plasmas have been observed to stop obeying ideal MHD during a phenomena known as magnetic reconnection. Magnetic reconnection is the annihilation of magnetic flux due to the overlap of oppositely directed field lines. One way magnetic reconnection can occur is when two ideal MHD plasmas with oppositely directed magnetic fields collide as in Figure 1a. Ideal magnetohydrodynamics says that magnetic flux is frozen into each plasma. In theory, this prevents the plasmas from merging and leads to the formation of a large magnetic field gradient as shown in 1b. This is because, if any particles flowed from one plasma into the other, they would drag the magnetic field with them according to Alfv́en's theorem. However, this magnetic field would immediately cancel with the oppositely directed magnetic field of the

other plasma. The absence of magnetic field at the merging site would then contradict Alfv́en's theorem. Consequently, plasmas with oppositely directed magnetic fields cannot merge within the framework of ideal MHD. However, studies of plasma merging have not detected a high magnetic field gradient as ideal MHD predicts. Instead, ideal MHD breaks down, the two distinct plasmas merge into one, and the field lines slip through the plasma and cancel with each other. This leads to the magnetic field geometry shown in Figure 1c. This is a change in magnetic topology, because the field lines in the independent plasmas before the merging were not connected. After the merging, those field lines are connected. The process is called magnetic reconnection, because the field lines of each plasma start separate, but when the plasmas merge, both plasmas' field lines break and then reconnect to form lines that span both plasmas as in Figure 1c.

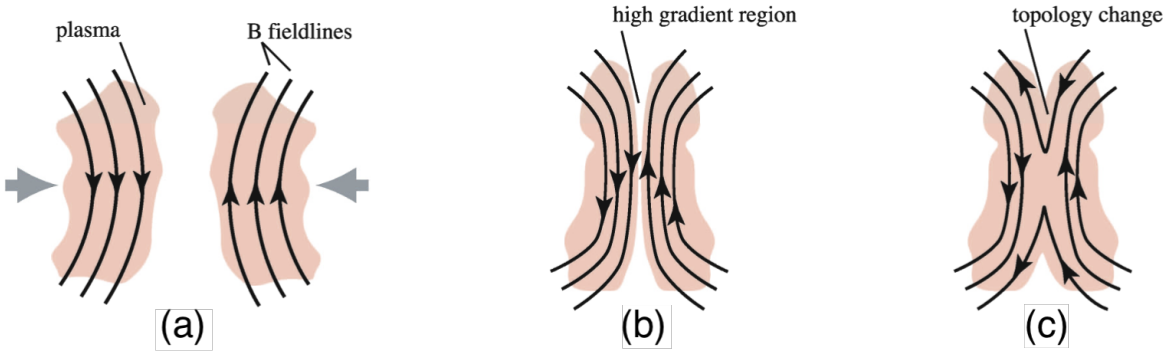

Figure 1: The merging of ideal MHD magnetized plasmas with oppositely directed magnetic fields. The prediction of ideal MHD and what is actually observed are shown. The predictions of ideal MHD do not agree with observation. (a): Two plasmas with frozen in flux. (b): Ideal MHD prediction of plasma collision. Plasmas cannot merge because merging would violate Alfv́en's theorem. The collision creates a high magnetic high gradient between the two plasmas. (c): Observed result of plasma collision. Plasmas merge and field lines reconnect causing a change in magnetic topology. [1]

The problem of magnetic reconnection can be phrased as follows: How can we modify ideal magnetohydrodynamics in order to allow it to describe magnetic reconnection? Which assumption that were made in deriving ideal MHD were incorrect in the conditions under which magnetic reconnection occurs?

Magnetic reconnection can be studied in both astrophysical plasmas and plasmas generated in the laboratory. Reconnection studies on astrophysical plasma usually have lower spatial resolution than measurements on laboratory plasmas, because spacecraft constellations designed to measure plasma activity consist of only a few spacecraft. For example, the Magnetospheric Multiscale, MMS, spacecraft constellation which is designed to study magnetic reconnection consists of only four spacecraft [2]. In laboratory reconnection experiments, on the other hand, plasma diagnostics can be used to attain measurements of plasma parameters at numerous locations. On the other hand, current laboratory reconnection experiments generate plasma with millimeter scale debye lengths, an important length scale for plasmas that will be described later. This makes it practically impossible for laboratory experiments to resolve reconnection dynamics on the scale of the debye length. Astrophysical plasma have long enough debye lengths that can be resolved by spacecraft constellations.

The first theoretical prediction of magnetic reconnection was made in 1957 by Sweet and Parker [3]. The predictions made by Sweet and Parker only apply to 2D magnetic reconnection [3]. A scenario is called 2D when all quantities are constant with respect to a single coordinate. That coordinate is ignorable, so only 2 coordinates are important. Since the Sweet-Parker model, there have been many theories on

2D magnetic reconnection but none on 3D magnetic reconnection. Due to the prevalence of theories on 2D reconnection and absence of 3D reconnection theories, laboratory experiments have almost exclusively studied 2D magnetic reconnection. Satellite measurements of reconnection in space plasmas are 3D, because astrophysical plasmas naturally have complex 3 dimensional magnetic geometries.

1.3 Study of 3D Magnetic Reconnection at SSX

The Swarthmore Spheromak Experiment (SSX) is a laboratory apparatus that generates plasma to study a wide range of plasma phenomena including magnetic reconnection [4, 5]. During the summer of 2023, we used the SSX device to study 3D magnetic reconnection. We produced and merged MHD plasmas called Taylor states to initiate 3D magnetic reconnection. The exact details of the experiment conducted as well as the results are the topic of much of this thesis. The summer 2023 SSX experiment are some of the first laboratory studies on 3D magnetic reconnection.

1.4 Organization of Thesis

Chapter 2 presents a sampling of plasma physics theory and the Sweet-Parker model of magnetic reconnection. Chapter 3 surveys previous studies on magnetic reconnection in laboratory plasmas. Chapter 4 discusses the summer 2023 SSX experimental setup including the plasma generation mechanism and diagnostics used. The thesis concludes by presenting the results of the summer 2023 SSX study on 3D magnetic reconnection in chapter 5, and provides concluding remarks in section 6. Future experiments that would build on the results of the summer 2023 SSX experiment are briefly discussed in chapter 7.

2 Plasma and Magnetic Reconnection Theory

In order to model a plasma, one could in principle write down $\mathbf{F} = m\mathbf{a}$ for each charged particle in the plasma with the net force being the sum of the electromagnetic force on the particle due to the electric field and magnetic field created by all other particles in the plasma and the mechanical forces on it due to collisions with other particles. Then, one could solve the equations to determine how each particle's position changes in time. However, even calculating the electric and magnetic fields due to the number of particles in a very simple plasma is so computationally intensive that is isn't feasible. For example, a 1 μg sample of fully ionized hydrogen plasma contains on the order of 10^{18} particles. The equation used to calculate the electric field of such a plasma at a single instant would have 2×10^{18} terms and would depend on the position, velocity, and acceleration of every particle in question. It is clear that another approach is necessary to describe plasma behavior.

There are three main models of plasma. In order of decreasing complexity they are the Vlasov model, the two-fluid model, and magnetohydrodynamics. The Vlasov model keeps track of the distribution of particle velocities at each point in space. The two-fluid model treats each species, electrons and different ions, as separate fluids. Magnetohydrodynamics treats the whole plasma as a single fluid. The two-fluid model can be derived from the Vlasov model when simplifying assumptions are made, and magnetohydrodynamics can be derived from the two-fluid model under further simplifying assumptions. Each model leads to different insights and is useful in different circumstances. In this thesis we will focus on magnetohydrodynamics, because as we will see in sections 2.7 and 2.8, it is the most relevant to understanding the problem of magnetic reconnection. We begin by discussing basic plasma physics concepts in sections 2.1 through 2.5 and then proceed to a discussion of magnetohydrodynamics in section 2.6. We will discuss the frozen-in-flux theorem and magnetic reconnection in sections 2.7 and 2.8. We will end with a description of two plasma geometries, the spheromak and the Taylor state, in section 2.9. These geometries that are important to understanding the 3D magnetic reconnection experiments carried out at the Swarthmore Spheromak Experiment in the summer of 2023.

2.1 Debye Shielding and Debye Length

Let us focus on a single electron in a plasma that is perturbed from equilibrium. The perturbation creates a local difference in electron and ion density which creates an electric field. The equation of motion for the electron is

$$m\frac{d\mathbf{v}}{dt} = q\mathbf{E} - \frac{\nabla p}{n} = 0 \tag{2.1}$$

where p is the plasma pressure, and n is the number density of electrons. $\frac{d\mathbf{v}}{dt} = 0$, because the flow is assumed to be steady. Now $\mathbf{E} = -\nabla\phi$ from the definition of ϕ. From the ideal gas law we have $p = nkT$. Substituting these into equation 2.1 gives

$$-q\nabla\phi - \frac{\nabla(nkT)}{n} = 0 \tag{2.2}$$

or

$$-q\nabla\phi = \frac{\nabla n}{n}kT \tag{2.3}$$

The perturbation from equilibrium can be treated as a radial perturbation. Since $\nabla = \hat{r}\frac{\partial}{\partial r} + ...$, we have

$$-q\frac{\partial \phi}{\partial r} = \frac{\partial n}{\partial r}\frac{kT}{n} \tag{2.4}$$

which is equivalent to

$$\frac{-q}{kT}d\phi = \frac{1}{n}dn \tag{2.5}$$

which can be solved to yield

$$n = n_0 e^{-q\phi/kT} \tag{2.6}$$

which gives the electron density as a function of electrostatic potential. Equation 2.6 is called the Boltzmann relation. [6]

Now focus on the electric field around any single electron or ion. Electrons in the plasma will move around in order to reduce or screen the charge's electric field. The ions, being much more massive than the electrons, move much more slowly than the ions and therefore do not participate in the screening. Another way of thinking of this screening effect is that the electrons move around to neutralize any accumulation of net charge. This effect is called Debye shielding. We can use Poisson's equation to find the potential near any particle

$$\nabla^2\phi = -\frac{\rho}{\epsilon_0} = -\frac{e}{\epsilon_0}(n_i - n_e) \tag{2.7}$$

Since the perturbation under consideration is in the electron density and not ion density, $n_i = n_0$, and we can use 2.6 and the fact that $e\phi << kT_i$ in a plasma in order to approximate the electron density as $n_e = n_0 e^{-e\phi/kT} \approx 1 - \frac{e\phi}{kT}$. Equation 2.7 can then be solved for the potential.

$$\begin{aligned}
\nabla^2\phi == -\frac{\rho}{\epsilon_0} &= -\frac{e}{\epsilon_0}(n_i - n_e) \\
&= -\frac{e}{\epsilon_0}(n_0 - n_0(1 - \frac{e\phi}{kT})) \\
&= -\frac{n_0 e^2 \phi}{kT\epsilon_0} \\
&= -\frac{\phi}{\lambda_D^2}
\end{aligned}$$

$$\phi(r) = \frac{\phi_0}{r}e^{-r/\lambda_D} \tag{2.8}$$

where $\lambda_D = \frac{kT\epsilon_0}{n_0 e^2}$ is the Debye length [7].

Equation 2.8 shows that close to a charge, for $r << \lambda_D$, $\phi \propto 1/r$, so the electric field of the charge is unshielded. Far from a charge, where $r >> \lambda_D$, $\phi = 0$, so the electric field of the charge completely shielded. From this analysis, we see that λ_D is the maximum length scale on which electric fields due to separation of charge exist in a plasma. External electric fields and electric fields due to induction can exist on scales larger than the debye length.

2.2 Single Particle Orbits

Consider an ion moving in a magnetized plasma. The magnetic field will make the particle move in circular orbits. We seek to determine the orbital angular speed ω_{ci} on scales larger than the Debye length. $\mathbf{E} = \mathbf{0}$ due to Debye shielding. To find ω_{ci} we use the Lorentz force formula $\mathbf{F} = q(\mathbf{E} + \mathbf{v} \times \mathbf{B})$, or since $\mathbf{E} = \mathbf{0}$

$$\mathbf{F} = q\mathbf{v} \times \mathbf{B} \tag{2.9}$$

We know the component of $\mathbf{v}$ that is parallel to $\mathbf{B}$ will cause the ion to move in a straight line in addition to its orbit. The component perpendicular to $\mathbf{B}$ will cause the ion to orbit. Let $\mathbf{v}_\perp$ be the component of velocity perpendicular to $\mathbf{B}$ and let $v_\perp = |\mathbf{v}_\perp|$. We equate the net force on the ion with the centripetal force to find the angular frequency of the ion's orbit, the ion cyclotron frequency ω_{ci}.

$$m\frac{v_\perp^2}{r} = qv_\perp B$$

$$\frac{qBr}{m} = v_\perp = r\omega_{ci}$$

$$\omega_{ci} = \frac{qB}{m} \tag{2.10}$$

The result $\omega_{ci} = \frac{qB}{m}$ shows that the angular frequency of an ion's orbit is independent of its initial velocity. Using the right hand rule to determine the direction of the ion orbits reveals that ions make left handed orbits about the magnetic field. [7]

One can also calculate the radius of the ion orbits in a plasma, the ion gyroradius $\rho_i = \frac{v_{th}}{\omega_{ci}}$. v_{th} is the ion thermal velocity, the velocity of an ion in a plasma. $v_{th} = \frac{kT_i}{m_i}$ where T_i is the ion temperature and m_i is the ion mass [8].

2.3 Plasma Frequency

A plasma consists of an approximately equal number of negative electrons and positive ions. We typically define n, the plasma density as $n = n_e = n_i$. For this reason, plasmas are approximately neutral overall. However, the thermal motion of electrons and ions can lead to the formation of net charges within a plasma. Suppose that due to the random thermal motion of particles, a separation of charge appears in the plasma. At a certain instant, some ions form a thin layer of positive charge of thickness δ which is adjacent to a thin layer of negative charge formed by the same number of electrons also of thickness δ. Since the layers of charge are very close together, we can approximate the electric field between the layers of charge as that of two infinite planes of charge, so $E = \frac{\sigma}{\epsilon_0} = \frac{ne\delta}{\epsilon_0}$ where σ is the charge density per unit area, e is the elementary charge, and n is the plasma density.

Both electrons and ions will experience a force from this electric field, but the electrons will respond to it much faster than the ions, because they have a much smaller mass. We can now write Newton's second law for the electrons subject to the electric field. M_e^{tot} is the total mass of the electrons in the negatively charged region, q is the charge of the negatively charged region, m_e is the mass of an electron, and V is the volume of the negatively charged region.

$$
\begin{aligned}
M_e^{tot} a &= qE \\
m_e n V \ddot{\delta} &= -neV\frac{ne\delta}{\epsilon_0} \\
\ddot{\delta} &= -\frac{ne^2}{m_e\epsilon_0}\delta \\
\ddot{\delta} &= -\omega_{pe}^2\delta \\
\delta &= Ae^{i\omega_{pe}t} + Be^{i\omega_{pe}t}
\end{aligned}
$$

where

$$\omega_{pe} = \sqrt{\frac{ne^2}{m_e\epsilon_0}} \tag{2.11}$$

is called the electron plasma frequency. The separation of charge in a plasma leads to an oscillation of the thickness of the charged regions. This occurs because electrons oscillate in response to the electric field created by the charge separation. ω_{pe} is the frequency of these electron oscillations [7].

During the derivation of ω_{pe}, we ignored the response of the ions to the electric field, because the ions have a much larger mass than the electrons. The ions, however, do respond to the electric field created by a separation of charge. The ions oscillate in response to the electric field just like the electrons. These ion oscillations occur at the ion plasma frequency ω_{pi} which has the formula

$$\omega_{pi} = \sqrt{\frac{nZ^2e^2}{m_i\epsilon_0}} \tag{2.12}$$

where Z is the charge of the ions and m_i is the ion mass.

2.4 Plasma β

$\beta = nk_BT/\frac{B^2}{\mu_0}$ is the dimensionless ratio of mechanical pressure to magnetic energy density. It characterizes the relative presence of kinetic energy and magnetic energy in a plasma as well as the relative importance of pressure forces and magnetic forces. When $\beta >> 1$, mechanical forces on the plasma dominate magnetic forces, and most of the plasma's energy is kinetic rather than magnetic. When $\beta << 1$, magnetic forces on the plasma dominate mechanical forces, and most of the plasma's energy in magnetic rather than kinetic.

2.5 Alfvén Speed and Alfvén Time

A magnetized plasma has energy stored in its magnetic field. Suppose the magnetic energy in a fluid element of volume dV is converted into energy of flow. If B and ρ are the magnitude of the magnetic field and the mass density at the fluid element's position respectively, we can find the speed of the outflowing plasma v using conservation of energy [7].

$$\frac{1}{2}\rho\ dV\ v^2 = \frac{B^2}{2\mu_0}dV$$
$$v = \frac{B}{\sqrt{\mu_0\rho}}$$

This speed is called the Alfvén speed, $v_A = \frac{B}{\sqrt{\mu_0\rho}}$. The Alfvén speed is the characteristic speed of disturbances in an MHD plasma. This is similar to how the sound speed in the characteristic speed of a disturbance in a gas or other media. The Alfvén time $\tau_A = \frac{\ell_{ch}}{v_A}$ is the system's characteristic length divided by the Alfvén speed. It is the characteristic time for a plasma that obeys magnetohydrodynamics which is detailed in the next section.

2.6 Magnetohydrodynamics

Magnetohydrodynamics, MHD, is the simplest of the three main models used to describe plasmas. Instead of describing each distinct species in a plasma, electrons, ions, and neutrals, separately, it treats the plasma as a single fluid. The MHD description of a plasma consists of five partial differential equations which will be referred to as the MHD equations. They can be solved for a given set of initial conditions and boundary conditions to yield the behavior of an MHD plasma. The MHD equations involve quantities from both classical fluid dynamics and classical electrodynamics. In MHD, the plasma is described by the mass density ρ, the fluid velocity field $\mathbf{u}$, the pressure $\mathbf{P}$, current density $\mathbf{J}$, as well as the electric and magnetic fields $\mathbf{E}$ and $\mathbf{B}$ [6]. MHD is a valid description of a plasma when

1. All length scales of interest are much greater than the Debye length.
2. The particle velocities are much smaller than the speed of light in a vacuum.
3. The time scales of interest are long compared to the ion and electron cyclotron periods.
4. The electron and ion gyroradii are much less than the size of the plasma.

In MHD, mass conservation is expressed by the equation

$$-\frac{\partial\rho}{\partial t} = \nabla\cdot(\rho\mathbf{u}) \tag{2.13}$$

The product $\rho\mathbf{u}$ represents the amount of mass flowing through a small cross sectional area. The negative sign in front of $\frac{\partial\rho}{\partial t}$ specifies that flow out of a location causes a decrease in density and flow into a location causes an increase in density.

The equation of state for an MHD plasma is

$$P/\rho^\gamma = \text{const} \tag{2.14}$$

where γ is the adiabatic constant 5/3.

The MHD equation of motion states that there are two forces on each differential volume element of the plasma, the magnetic $\mathbf{J}\times\mathbf{B}$ force and the pressure gradient force, $-\nabla P$.

$$\rho\frac{D\mathbf{u}}{Dt} = \mathbf{J}\times\mathbf{B} - \nabla P \tag{2.15}$$

Note that there is no electric force on a fluid element. This is because MHD only applies when all lengths of consideration are more than λ_D which implies that the electric field is screened out by Debye shielding.

The operator $\frac{D}{Dt} = \frac{\partial}{\partial t} + \mathbf{u} \cdot \nabla$ is called the convective derivative. To understand why the convective derivative is used instead of a regular partial derivative, consider an arbitrary vector property of a fluid $\mathbf{A}(\mathbf{x}, t)$. $\mathbf{A}$ at a specific location can change in time in two ways. It can either change explicitly with time, or it can change due to a change in location. From the chain rule we have

$$\frac{d\mathbf{A}(\mathbf{x},t)}{dt} = \frac{\partial A}{\partial t} + \frac{\partial A}{\partial x}\frac{\partial x}{\partial t} + \frac{\partial A}{\partial y}\frac{\partial y}{\partial t} + \frac{\partial A}{\partial z}\frac{\partial z}{\partial t} \tag{2.16}$$

or

$$\frac{d\mathbf{A}(\mathbf{x},t)}{dt} = \mathbf{u} \cdot \nabla \mathbf{A} \tag{2.17}$$

so we define $\frac{D}{Dt} = \frac{\partial}{\partial t} + \mathbf{u} \cdot \nabla$ to be the convective derivative

Another important relationship in MHD is MHD Ohm's law. It describes the ability for electric and magnetic fields to produce currents in a plasma.

$$\mathbf{E} + \mathbf{u} \times \mathbf{B} = \eta \mathbf{J} \tag{2.18}$$

where η is the resistivity of the plasma. This equation is usually not stated as one of the MHD equations. Instead, we take its curl to yield equation 2.19, the MHD induction equation. Note that two of Maxwell's equations, Faraday's Law $\nabla \times \mathbf{E} = -\frac{\partial \mathbf{B}}{\partial t}$ and no magnetic monopoles $\nabla \cdot \mathbf{B} = 0$ are used in the derivation of the induction equation from MHD Ohm's law.

$$\begin{aligned}
\nabla \times (\mathbf{E} + \mathbf{u} \times \mathbf{B}) &= \nabla \times (\eta \mathbf{J}) \\
\nabla \times \mathbf{E} + \nabla \times (\mathbf{u} \times \mathbf{B}) &= -\frac{\eta}{\mu_0} \nabla \times (\nabla \times \mathbf{B}) \\
\nabla \times \mathbf{E} + \nabla \times (\mathbf{u} \times \mathbf{B}) &= -\frac{\eta}{\mu_0} (\nabla (\nabla \cdot \mathbf{B}) - \nabla^2 \mathbf{B}) \\
-\frac{\partial \mathbf{B}}{\partial t} + \nabla \times (\mathbf{u} \times \mathbf{B}) &= -\frac{\eta}{\mu_0} \nabla^2 \mathbf{B}
\end{aligned}$$

and finally

$$\frac{\partial \mathbf{B}}{\partial t} = \nabla \times (\mathbf{u} \times \mathbf{B}) + \frac{\eta}{\mu_0} \nabla^2 \mathbf{B} \tag{2.19}$$

We can compare the importance of the convective term $\nabla \times (\mathbf{u} \times \mathbf{B})$ and the resistive term $\frac{\eta}{\mu_0} \nabla^2 \mathbf{B}$ via a quantity called the magnetic Reynolds number R_m.

$$\begin{aligned}
R_m &= \frac{|\nabla \times (\mathbf{u} \times \mathbf{B})|}{|\frac{\eta}{\mu_0} \nabla^2 \mathbf{B}|} \\
&= \frac{v_{ch} B / \ell_{ch}}{\eta B / \mu_0 \ell_{ch}^2} \\
&= \frac{\mu_0 v_{ch} \ell_{ch}}{\eta}
\end{aligned}$$

where v_{ch} and ℓ_{ch} are the characteristic speed and lengths associated with the MHD processes in question.

The final MHD equation is Ampére's law

$$\nabla \times \mathbf{B} = \mu_0 \mathbf{J} + \mu_0 \epsilon_0 \frac{\partial \mathbf{E}}{\partial t} \tag{2.20}$$

However, under the assumptions of MHD, the displacement current $\mu_0 \epsilon_0 \frac{\partial \mathbf{E}}{\partial t}$ is negligible. To see this, we compare the magnitudes of the $\mu_0 \epsilon_0 \frac{\partial \mathbf{E}}{\partial t}$ and $\nabla \times \mathbf{B}$. To make this comparison we introduce ℓ_{ch}, t_{ch}, and v_{ch} the characteristic length, time, and velocity for phenomena we are trying to describe with MHD. Note that $v_{ch} = \ell_{ch}/t_{ch}$ We begin by estimating E using Faraday's law, $\nabla \times \mathbf{E} = -\frac{\partial \mathbf{B}}{\partial t}$.

$$E/\ell_{ch} \approx B/t_{ch} \tag{2.21}$$

$$E \approx B \cdot \ell_{ch}/t_{ch} \tag{2.22}$$

We now use the approximation of E to approximate the magnitude of the displacement current.

$$\frac{\mu_0 \epsilon_0 |\frac{\partial \mathbf{E}}{\partial \mathbf{t}}|}{|\nabla \times \mathbf{B}|} \approx \frac{c^{-2} E/t_{ch}}{B/\ell_{ch}} \tag{2.23}$$

$$\frac{\mu_0 \epsilon_0 |\frac{\partial \mathbf{E}}{\partial \mathbf{t}}|}{|\nabla \times \mathbf{B}|} \approx \frac{\ell_{ch}^2/t_{ch}^2}{c^2} = \left(\frac{v_{ch}}{c}\right)^2 \tag{2.24}$$

Therefore, as long as the characteristic speed of the processes in question is much less than c, the displacement current can be neglected. We assumed that this condition holds for an MHD plasma. Therefore the displacement current can be neglected and Ampère's law can be simplified to

$$\nabla \times \mathbf{B} = \mu_0 \mathbf{J} \tag{2.25}$$

2.6.1 Resistive vs Ideal Magnetohydrodynamics

We have now discussed all of the MHD equations. There are 11 total unknowns, ρ, P, and the three components of each of $\mathbf{u}$, $\mathbf{J}$, and $\mathbf{B}$. $\gamma = 5/3$ and η are constants. There are 11 equations, 2 scalar equations and 3 three-dimensional vector equations, which makes the system solvable. The MHD equations are listed below for completeness.

$$-\frac{\partial \rho}{\partial t} = \nabla \cdot (\rho \mathbf{u}) \tag{2.26}$$

$$P/\rho^\gamma = \text{const} \tag{2.27}$$

$$\rho \frac{D\mathbf{u}}{Dt} = \mathbf{J} \times \mathbf{B} - \nabla P \tag{2.28}$$

$$\frac{\partial \mathbf{B}}{\partial t} = \nabla \times (\mathbf{u} \times \mathbf{B}) + \frac{\eta}{\mu_0} \nabla^2 \mathbf{B} \tag{2.29}$$

$$\nabla \times \mathbf{B} = \mu_0 \mathbf{J} \tag{2.30}$$

While Faraday's law and $\nabla \cdot \mathbf{B} = 0$ are not explicitly listed, they are used to derive equation 2.29, the induction equation, and therefore should be thought of as part of MHD. The above equations include the resistive term $\frac{\eta}{\mu_0} \nabla^2 \mathbf{B}$ in the induction equation, so the model they describe is called resistive magnetohy-

drodynamics. When the resistivity of a plasma is small, the resistive term $\frac{\eta}{\mu_0}\nabla^2\mathbf{B}$ in the induction equation can be dropped. Doing so simplifies resistive MHD to ideal MHD. Ideal MHD is resistive MHD with $\eta = 0$. The ideal MHD equations are included below for completeness.

$$-\frac{\partial \rho}{\partial t} = \nabla \cdot (\rho \mathbf{u}) \tag{2.31}$$

$$P/\rho^{\gamma} = \text{const} \tag{2.32}$$

$$\rho \frac{D\mathbf{u}}{Dt} = \mathbf{J} \times \mathbf{B} - \nabla p \tag{2.33}$$

$$\frac{\partial \mathbf{B}}{\partial t} = \nabla \times (\mathbf{u} \times \mathbf{B}) \tag{2.34}$$

$$\nabla \times \mathbf{B} = \mu_0 \mathbf{J} \tag{2.35}$$

2.7 Frozen in Flux Theorem

A plasma with very small resistivity can be modelled with ideal MHD. An important consequence of ideal MHD is the frozen-in flux theorem which is also known as Alfvén's theorem. The theorem states that the flux through a loop that moves with the fluid in a perfectly conducting plasma is constant. In terms of field lines, the frozen-in-flux condition means that the number of field lines piercing through a loop in a perfectly conducting plasma is constant. The frozen-in flux condition can be intuitively understood as requiring that the magnetic field lines in a perfectly conducting plasma bend and twist with the plasma as it moves. The frozen-in flux theorem is now formally stated and proved following Griffiths [9].

Frozen-in flux theorem: Let P be a loop in a perfectly conducting plasma at time t which encloses the surface S. The loop P moves with the velocity field of the plasma $\mathbf{u}$. Let P' be the loop at time $t + dt$, and let S' be the surface enclosed by P'. Then the magnetic flux through the loop is constant.

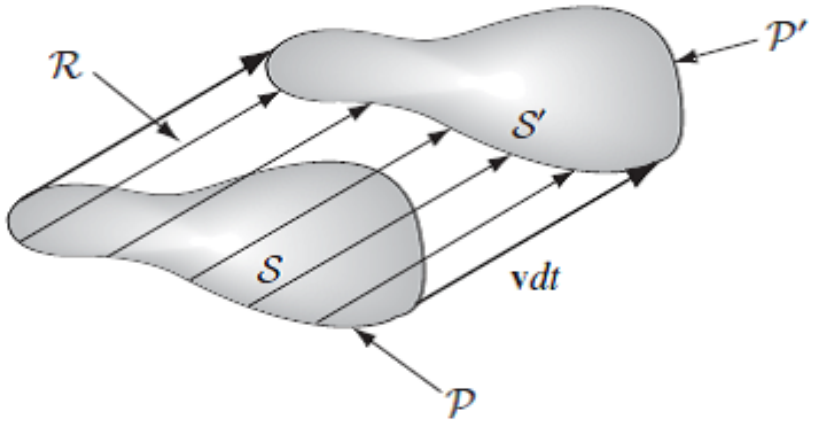

Figure 2: A loop that flows with the velocity field of a plasma [9]. At time t, the loop is called P. At time $t + dt$ the loop is called P'. The surface S is enclosed by P, and the surface S' is enclosed by P. The ribbon surface R is traced out by the path the loop moves through in time dt. If the plasma has zero resistivity, the magnetic flux through the loop is constant.

Proof: The magnetic flux through P' and P are

$$\int_{S'} \mathbf{B}(t+dt) \cdot d\mathbf{a} \tag{2.36}$$

and

$$\int_{S} \mathbf{B}(t) \cdot d\mathbf{a} \tag{2.37}$$

respectively. Therefore the change in flux $d\phi$ through the loop in time dt is

$$d\phi = \int_{S'} \mathbf{B}(t+dt) \cdot d\mathbf{a} - \int_{S} \mathbf{B}(t) \cdot d\mathbf{a} \tag{2.38}$$

Taking the integral of $\nabla \cdot \mathbf{B} = 0$ over an arbitrary volume V we get

$$\int_{V} \nabla \cdot \mathbf{B} \; dV = \int_{V} 0 \; dV = 0 \tag{2.39}$$

Using Gauss's theorem we have that

$$\int_{\partial V} \mathbf{B} \cdot d\mathbf{a} = 0 \tag{2.40}$$

where ∂V is the surface that encloses V. As the loop moves through space with velocity $\mathbf{u}$, it traces out a ribbon surface R as shown in Figure 2. Now we apply equation 2.40 to the volume enclosed by S, S', and R at time $t + dt$

$$\int_{S'} \mathbf{B}(t+dt) \cdot d\mathbf{a} + \int_{R} \mathbf{B}(t+dt) \cdot d\mathbf{a} - \int_{S} \mathbf{B}(t+dt) \cdot d\mathbf{a} = 0 \tag{2.41}$$

Substituting $\int_{S'} \mathbf{B}(t+dt) \cdot d\mathbf{a} = d\phi + \int_{S} \mathbf{B}(t) \cdot d\mathbf{a}$ we get

$$d\phi + \int_{S} \mathbf{B}(t) \cdot d\mathbf{a} + \int_{R} \mathbf{B}(t+dt) \cdot d\mathbf{a} - \int_{S} \mathbf{B}(t+dt) \cdot d\mathbf{a} = 0 \tag{2.42}$$

$$d\phi = -\int_{R} \mathbf{B}(t+dt) \cdot d\mathbf{a} + \int_{S} [\mathbf{B}(t+dt) - \mathbf{B}(t)] \cdot d\mathbf{a} \tag{2.43}$$

$$d\phi = -\int_{R} \mathbf{B}(t+dt) \cdot d\mathbf{a} + dt \int_{S} \frac{\mathbf{B}(t+dt) - \mathbf{B}(t)}{dt} \cdot d\mathbf{a} \tag{2.44}$$

$$d\phi = -\int_{R} \mathbf{B}(t+dt) \cdot d\mathbf{a} + dt \int_{S} \frac{\partial \mathbf{B}(t)}{\partial t} \cdot d\mathbf{a} \tag{2.45}$$

The term $\int_{R} \mathbf{B}(t+dt) \cdot d\mathbf{a}$ can be written differently. We can see from Figure 2 that $d\mathbf{a} = d\mathbf{l} \times \mathbf{u}dt$ where $d\mathbf{l}$ is a differential element of P. Now expand $\int_{R} \mathbf{B}(t+dt) \cdot d\mathbf{a}$ in a Taylor series about time t.

$$\int_R \mathbf{B}(t+dt)\cdot d\mathbf{a} = \tag{2.46}$$

$$\int_R (\mathbf{B}(t) + dt\frac{\partial \mathbf{B(t)}}{\partial t} + \mathcal{O}(dt^2))\cdot(d\mathbf{l}\times\mathbf{u}dt) = \tag{2.47}$$

$$\int_R \mathbf{B}(t)\cdot(d\mathbf{l}\times\mathbf{u}dt) + dt\frac{\partial \mathbf{B(t)}}{\partial t}\cdot(d\mathbf{l}\times\mathbf{u}dt) + \mathcal{O}(dt^2)\cdot(d\mathbf{l}\times\mathbf{u}dt) \tag{2.48}$$

where $\mathcal{O}(dt^2)$ is an infinite series that depends on powers of dt beyond 1. All terms involving a power of dt beyond the first are negligible, so we can say

$$\int_R \mathbf{B}(t+dt)\cdot d\mathbf{a} = \int_R \mathbf{B}(t)\cdot(d\mathbf{l}\times\mathbf{u}dt) \tag{2.49}$$

Now substitute equation 2.48 into equation 2.45, use a vector identity, and use Stokes' theorem.

$$d\phi = -\int_R \mathbf{B}(t)\cdot(d\mathbf{l}\times\mathbf{u}dt) + dt\int_S \frac{\partial \mathbf{B}}{\partial t}\cdot d\mathbf{a} \tag{2.50}$$

$$= -dt\int_P (\mathbf{u}\times\mathbf{B}(t))\cdot d\mathbf{l} + dt\int_S \frac{\partial \mathbf{B}}{\partial t}\cdot d\mathbf{a} \tag{2.51}$$

$$= -dt\int_S \nabla\times(\mathbf{u}\times\mathbf{B}(t))\cdot d\mathbf{a} + dt\int_S \frac{\partial \mathbf{B}}{\partial t}\cdot d\mathbf{a} \tag{2.52}$$

$$\frac{d\phi}{dt} = \int_S \left[\frac{\partial \mathbf{B}}{\partial t} - \nabla\times(\mathbf{u}\times\mathbf{B}(t))\right]\cdot d\mathbf{a} \tag{2.53}$$

MHD Ohm's law states that $\eta\mathbf{J} = \mathbf{E} + \mathbf{u}\times\mathbf{B}$. In the case that the plasma is perfectly conducting, $\eta = 0$. This allows us to write the ideal MHD Ohm's law

$$\mathbf{E} + \mathbf{u}\times\mathbf{B} = \mathbf{0} \tag{2.54}$$

Taking the curl of the 2.54 and using Faraday's law to substitute for $\nabla\times\mathbf{E}$, we can see that

$$-\frac{\partial \mathbf{B}}{\partial t} + \nabla\times(\mathbf{u}\times\mathbf{B}) = \mathbf{0} \tag{2.55}$$

Substituting equation 2.55 into equation 2.53 yields

$$\frac{d\phi}{dt} = \int_S \mathbf{0}\cdot d\mathbf{a} = 0 \tag{2.56}$$

so ϕ, the flux through the loop, is constant.

The frozen-in flux theorem is a remarkable result of ideal MHD and allows for a simple understanding of the relationship between the fluid flow and magnetic field in an ideal MHD plasma. It does not, however, apply in situations where ideal MHD breaks down such as during magnetic reconnection.

2.8 Magnetic Reconnection

Magnetic reconnection is the process by which magnetic flux in a plasma is annihilated. When two highly conductive plasmas are separated from each other by a large distance, as in Figure 3a, each of their motions can be described by ideal MHD. The frozen-in flux condition proved in the last section applies to each of the plasmas independently.

When two plasmas with oppositely directed magnetic fields move towards each other, ideal MHD does not predict that the plasmas merge together. Instead, it predicts the formation of a large magnetic field gradient as shown in Figure 3b. To see this, assume that ideal MHD accurately describes the merging of plasmas with oppositely directed magnetic fields. In this case, the frozen-in flux condition must hold. If the plasmas were to merge together then according to Alfvén's theorem, the oppositely directed magnetic fields would be pulled into the merging region which causes them to cancel. A loop inside either plasma before the merging would have significant flux through it, but once the merging occurs, the loop would be inside the merging region. Since the magnetic fields have cancelled there, there is no flux through the loop. This is a violation of the frozen-in flux condition. This means that if ideal MHD were to apply to the described merging, the plasmas would not be able to merge. Instead, we would see a large magnetic field gradient as indicated in Figure 3b.

The large magnetic field gradient predicted by ideal MHD is not observed. Instead, ideal MHD breaks down, the plasmas merge together, and the frozen-in flux condition is violated. The opposing field lines can be said to slip through the plasma. The field lines overlap and annihilate as in Figure 1c. The annihilation of the magnetic fields causes the conversion of magnetic energy to other forms of energy and a change in magnetic topology. We say that the magnetic field has changed topology because before the merging, each plasmas had independent field lines that did not intersect the magnetic field of the other plasma. After the merging, the field lines span both plasmas as in Figure 3c. The magnetic field lines can be said to break and then reconnect together. This process is known as magnetic reconnection.

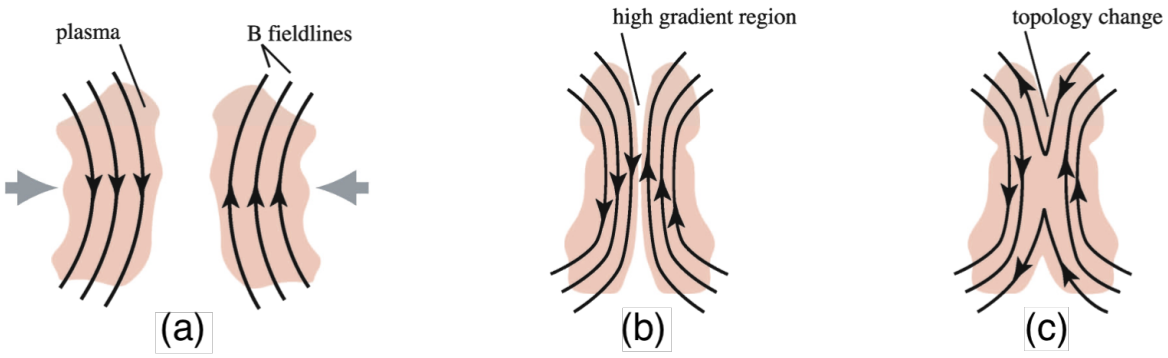

Figure 3: This figure is the same as Figure 1 and is repeated for convenience. The merging of ideal MHD magnetized plasmas with oppositely directed magnetic fields. The prediction of ideal MHD and what is actually observed are shown. The predictions of ideal MHD do not agree with observation. (a): Two plasmas with frozen in flux. (b): Ideal MHD prediction of plasma collision. Plasmas cannot merge because merging would violate Alfvén's theorem. The collision creates a high magnetic high gradient between the two plasmas. (c): Observed result of plasma collision. Plasmas merge and field lines reconnect causing a change in magnetic topology. [1]

Determining the outcome of a reconnection event is an unsolved problem in plasma physics. There is currently no universal model that accurately predicts the outcome of magnetic reconnection observed in astrophysical and laboratory plasmas. There are models that predict the outcome of reconnection under specific conditions, but no existing model is able to predict the outcome of reconnection in all conditions. Some questions relevant to the problem of reconnection are: What assumption or assumptions that were made in deriving ideal MHD are violated during magnetic reconnection? Where does the energy stored in the annihilated magnetic field go? What are dimensions of the reconnection layer, the region between the merging plasmas where reconnection takes place?

2.8.1 Sweet-Parker Reconnection

The first model of magnetic reconnection was proposed by Sweet and Parker in 1957 [3]. It provides an explanation for magnetic reconnection using resistive MHD. The model assumes that reconnection is a steady state process, the plasmas undergoing reconnection are incompressible, and all magnetic energy in the incoming plasmas is converted to kinetic energy. It is also a 2D model which means that it models reconnection with a single ignorable coordinate. We now present the Sweet-Parker model of magnetic reconnection [7, 10].

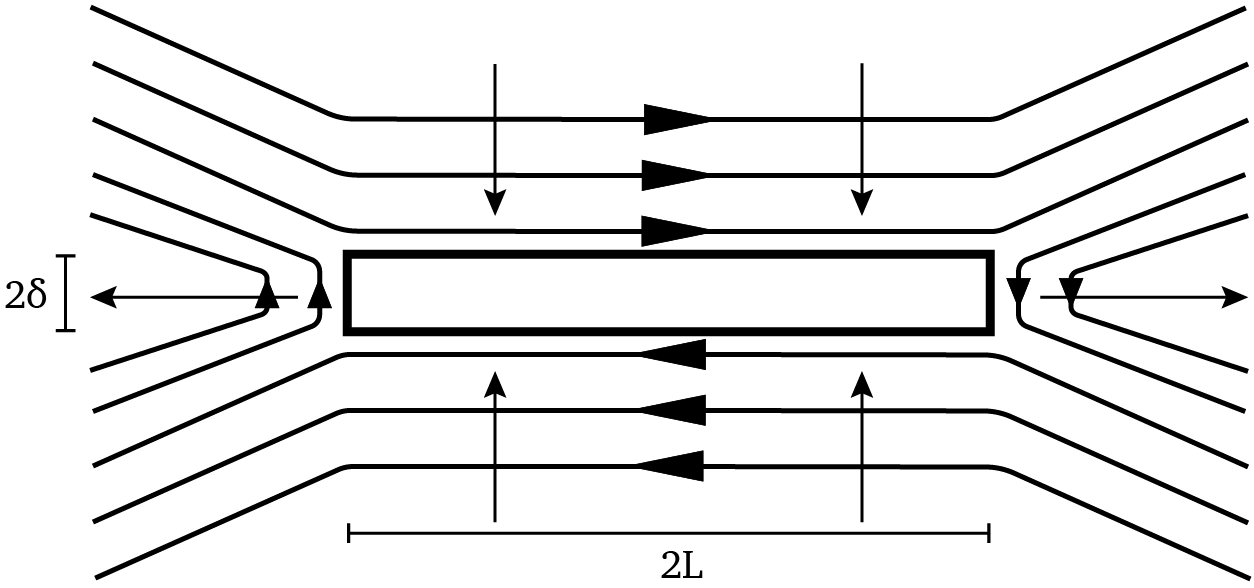

Figure 4: The Sweet-Parker model of magnetic reconnection. The model is 2D, because the situation does not vary in the out of plane direction, z. Plasmas with oppositely directed magnetic fields enter the reconnection layer and exit out its sides. Magnetic energy is entirely converted to flow velocity.

Two identical plasmas with oppositely directed uniform magnetic fields of magnitude B enter the reconnection layer of length $2L$ and width 2δ with speed v_{in}. Plasma leaves the reconnection layer with speed v_{out}. The plasma does not vary in the z direction which makes this model 2D.

Since the plasmas are incompressible $\rho =$ constant. The continuity equation then simplifies to

$$\rho \nabla \cdot \mathbf{v} = 0 \tag{2.57}$$

$$\int_V \nabla \cdot \mathbf{v} \cdot dV = 0 \tag{2.58}$$

where V is a volume. By the divergence theorem we have

$$\int_S \mathbf{v} \cdot d\mathbf{a} = 0 \tag{2.59}$$

where S is the surface bounding V. Now take the volume V to be the reconnection layer and z_0 to be the length of the plasmas in the z-direction.

$$-v_{in} 2Lz_0 - v_{in} 2Lz_0 + v_{out} 2\delta z_0 + v_{out} 2\delta z_0 = 0 \tag{2.60}$$

$$\frac{v_{in}}{v_{out}} = \frac{\delta}{L} \tag{2.61}$$

Next we recognize that there is no current in the each region containing an inflowing plasma, because $\nabla \times \mathbf{B} = \mu_0 \mathbf{J}$ and $\mathbf{B}$ is constant in each inflow region. Then from resistive MHD Ohm's law $\mathbf{E} + \mathbf{v} \times \mathbf{B} = \eta \mathbf{J}$ we find that in both inflowing plasmas

$$\mathbf{E}_{in} = -v_{in} B \hat{z} \tag{2.62}$$

The inflowing plasmas enter the reconnection layer at the same speed and merge in the reconnection layer, so the flow velocity in the reconnection layer is zero by conservation of momentum. Therefore, by Ohm's law,

$$\mathbf{E}_{layer} = \eta \mathbf{J} \tag{2.63}$$

Since we are assuming that reconnection is a steady state process, $\frac{\partial \mathbf{B}}{\partial t} = 0$. Using a loop in the y-z plane to apply Faraday's law we find that

$$\mathbf{E}_{in} = \mathbf{E}_{layer} \tag{2.64}$$

By symmetry, contributions to the line integral from the electric field in the y direction in the reconnection layer as well as in the inflow plasma sum to zero. Now combining equations 2.62, 2.63, and 2.64 we have

$$v_{in} B = \eta J \tag{2.65}$$

The final piece of information needed to solve the Sweet-Parker model is obtained by using Ampère's law along the boundary of the reconnection region. The magnetic field of the outflowing fluid is negligible, because reconnection is assumed to convert all incoming magnetic energy to kinetic energy.

$$\int \mathbf{B} \cdot d\mathbf{l} = \mu_0 I \tag{2.66}$$

$$4BL = 4\mu_0 JL\delta \tag{2.67}$$

$$\frac{B}{J} = \mu_0 \delta \tag{2.68}$$

Now we can calculate the Sweet-Parker model's predictions about the reconnection process. First combine equations 2.65 and 2.68 to yield

$$\mu_0 \delta = \frac{\eta}{v_{in}} \tag{2.69}$$

$$\frac{\mu_0 v_{in} \delta}{\eta} = 1 \tag{2.70}$$

Recall the definition of magnetic Reynolds number $R_m = \frac{\mu_0 v_{ch} \ell_{ch}}{\eta}$. Equation 2.70 shows that the Parker model predicts that the magnetic Reynolds number during reconnection is 1. This means that convection balances diffusion. We have found that the width of the reconnection layer as a function of conductivity and inflow speed. Specifically, the width of the reconnection layer is adjusted to make the magnetic Reynolds number equal to 1.

Next we are interested in predicting the reconnection rate which is defined as the ratio of the inflow speed to the outflow speed $\frac{v_{in}}{v_{out}}$. To begin, we solve for v_{out} using conservation of energy. Since the reconnection process is assumed to convert all magnetic energy to kinetic energy, the outflow speed must be much greater than the inflow speed.

$$\frac{1}{2}\rho v_{in}^2 + \frac{B_{in}^2}{2\mu_0} = \frac{1}{2}\rho v_{out}^2 + \frac{B_{out}^2}{2\mu_0} \tag{2.71}$$

$$\frac{B_{in}^2}{2\mu_0} \approx \frac{1}{2}\rho v_{out}^2 \tag{2.72}$$

$$v_{out} = \frac{B}{\sqrt{\mu_0 \rho}} = v_A, \text{ the Alfvén speed} \tag{2.73}$$

Therefore by equations 2.61, 2.70, and 2.73, the squared reconnection rate is $\left(\frac{v_{in}}{v_A}\right)^2 = \left(\frac{\delta}{L}\right)\left(\frac{\eta}{\mu_0 \delta v_A}\right)$. We define the Lundquist number S as

$$S = \frac{\mu_0 v_A L}{\eta} \tag{2.74}$$

So the predicted reconnection rate can be written as

$$\frac{v_{in}}{v_{out}} = \frac{1}{\sqrt{S}} \tag{2.75}$$

A reconnection rate of 0.1 has been observed in many experiments and simulations [11]. While the development of the Sweet-Parker model was an important first step in understanding magnetic reconnection, the reconnection rates that it predicts are much smaller than observed in astrophysical plasmas [12]. It also does not account for the ion heating which has been routinely observed in laboratory reconnection

experiments [13]. Another drawback of the Sweet-Parker model is that it only considers a 2D scenario even though reconnection can occur when quantities vary in all three directions.

2.9 MHD Equilibrium, the Spheromak, and the Taylor State

2.9.1 Force-Free States

We are often interested in configurations of plasmas with no forces acting on them. These states are called force-free states. Let us consider a low β MHD plasma. According to the MHD equation of motion, there are two forces that can act the plasma, $-\nabla P$ and $\mathbf{J} \times \mathbf{B}$. Since the plasma has low β, pressure forces are negligible, $-\nabla P \to 0$. This means that a force free state must have $\mathbf{J} \times \mathbf{B} = \mathbf{0}$. This only occurs when $\mathbf{J} \parallel \mathbf{B}$ which is equivalent to

$$\mathbf{J} = \lambda \mathbf{B} \tag{2.76}$$

for some λ which can depend on spatial coordinates. Using the simplified Ampère's law from MHD, $\nabla \times \mathbf{B} = \mu_0 \mathbf{J}$, we have

$$\frac{\nabla \times \mathbf{B}}{\mu_0} = \lambda \mathbf{B} \tag{2.77}$$

$$\nabla \times \mathbf{B} = \lambda \mathbf{B} \tag{2.78}$$

This simple derivation of equation 2.78, the force free condition, allows for spatial variation in λ. However, force-free states have values of λ with no spatial variation [14]. The full derivation of constant λ is not included for the sake of brevity, but I will briefly describe it. A force-free state is a state with a local minimum of magnetic energy. It can be shown that when MHD plasmas relax into their lowest energy state, a quantity called magnetic helicity is conserved [14]. Magnetic helicity K is defined by

$$K = \int_V \mathbf{A} \cdot \mathbf{B} \, dV \tag{2.79}$$

where $\mathbf{A}$ is the magnetic vector potential such that $\nabla \times \mathbf{A} = \mathbf{B}$. The minimization of magnetic energy subject to constant magnetic helicity can be performed using Lagrange multipliers. The result is $\nabla \times \mathbf{B} = \lambda \mathbf{B}$ with constant λ [14]. Once we have $\mathbf{B}$ for a force free state, we can find $\mathbf{J}$ using $\nabla \times \mathbf{B} = \mu_0 \mathbf{J}$.

2.9.2 Spheromaks and Taylor states

The term spheromak refers to a specific configuration of plasma, including its magnetic field. The magnetic field of a spheromak satisfies the force-free equation $\nabla \times \mathbf{B} = \lambda \mathbf{B}$. When the force-free equation is solved inside a cylinder of radius R and length L one gets infinitely many solutions, one for each possible value of λ. The axisymmetric solution where λ is commonly denoted as λ_0 is

$$B_r = B_0 \frac{k_z}{k_r} J_1(k_r r) \cos(k_z z) \tag{2.80}$$

$$B_\phi = B_0 \frac{\lambda_0}{k_r} J_1(k_r r) \sin(k_z z) \tag{2.81}$$

$$B_z = B_0 J_0(k_r r) \sin(k_z z) \tag{2.82}$$

$$\text{where } k_r = \frac{3.83}{R} \quad k_z = \frac{\pi}{L} \quad \lambda_0 = \sqrt{k_r^2 + k_z^2} \tag{2.83}$$

where J_0 and J_1 are Bessel functions. The number 3.83 appears in equation 2.83, because it is the first zero of J_1 [15]. Note that we can calculate $\mathbf{J}$ for this solution using $\mu_0 \mathbf{J} = \nabla \times \mathbf{B} = \lambda \mathbf{B}$. This solution to the force-free equation is called a spheromak and it is shown in Figure 5. The magnetic field in a spheromak is commonly broken down into a toroidal component and a poloidal component. The ϕ component of the magnetic field is called the toroidal field, because it points around the torus. The r and z components of the magnetic field are together called the poloidal field, because they points between the poles of the cylinder.

The experiment detailed later in this thesis involves shooting spheromaks down long flux conservers, copper tubes which the magnetic field and plasma cannot penetrate. While the spheromak is a force free state, it is an unstable equilibrium state. A small perturbation of a spheromaks's magnetic field will make it tilt and twist into a twisted rope magnetic geometry called a Taylor state [16]. The details of a spheromak's evolution into a Taylor state are beyond the scope of this thesis because the process involves MHD turbulence. Nevertheless, when a spheromak moves down a flux conserver, it tilts and twists into a Taylor state. A diagram of the magnetic field of a Taylor state is shown in Figure 6. Like spheromaks, Taylor states are force free structures which satisfy $\nabla \times \mathbf{B} = \lambda \mathbf{B}$. But unlike spheromaks, Taylor states are stable equilibrium states. The magnetic field of a Taylor state does have an analytical form involving Chandrasekhar-Kendall functions [17]. It is omitted here, because the equations are too complex to visualize or yield physical intuition.

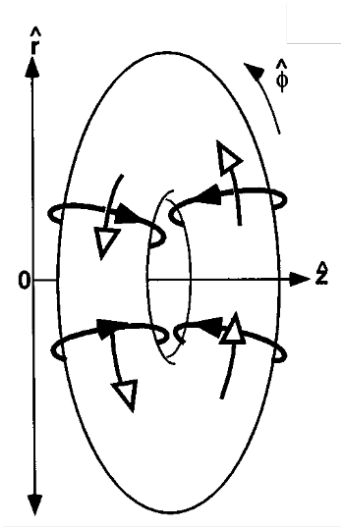

Figure 5: A diagram of a spheromak, the axisymmetric solution to the force-free equation in a cylinder, showing the direction of the toroidal and poloidal magnetic field. The toroidal field is shown with open arrows and the poloidal field is shown with filled in arrows [15].

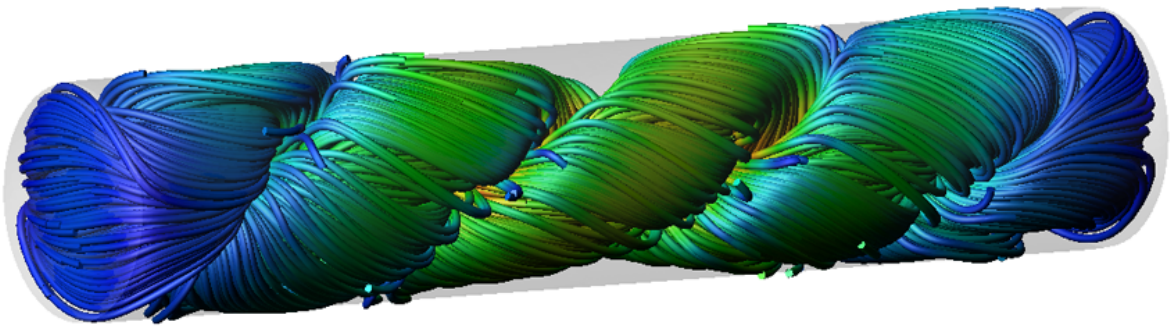

Figure 6: A diagram of a Taylor state, a twisted rope magnetic geometry of magnetized MHD plasmas constrained within a cylinder. The magnetic field points along the lines in the image. A Taylor state is a stable force free state.

3 Prior Studies of Magnetic Reconnection

3.1 Stenzel and Gekelman

The first experiments on magnetic reconnection were done at UCLA by Stenzel and Gekelman starting in 1979 and throughout the 1980s [10]. The apparatus, shown is Figure 7, consisted of a 2 meter long cylindrical metal chamber with a diameter of 1 meter which was evacuated and filled with 10^{-4} Torr of either argon or helium depending on the experiment [18]. A uniform density $n_e \approx 10^{12}$ cm^{-3} plasma is generated by heating an oxide-coated cathode and continuously pulsing a discharge voltage between the cathode and a nearby mesh anode. An axial magnetic field is created by coils around the main chamber. To create a reconnection event, an additional 20 kA current is pulsed through two parallel metal plates which are equidistant from the center of the machine. Typical temperatures observed were $kT_e = 10kT_i = 4$ eV. The ion gyroradius in this experiment was similar to the radius of the chamber which means that the plasma is not an MHD plasma.

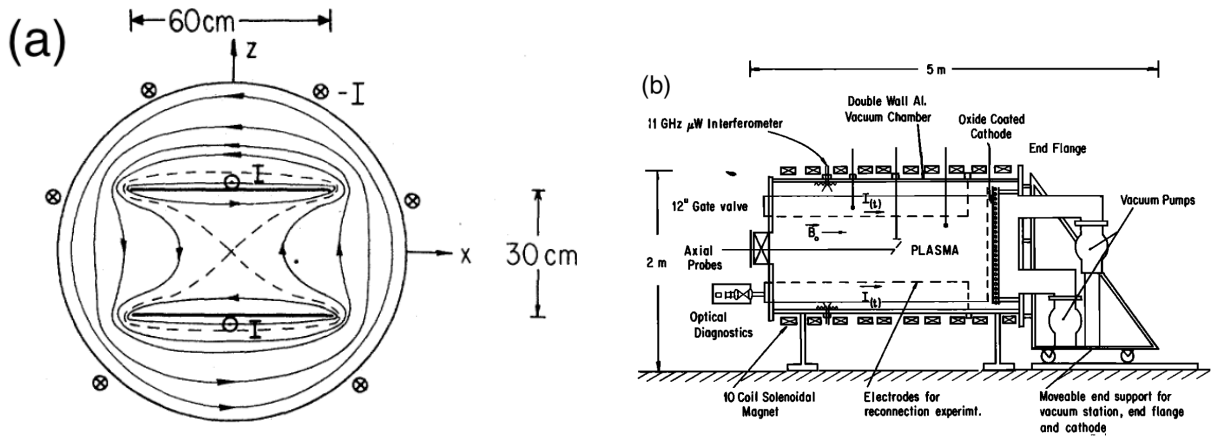

Figure 7: (a) The cross sectional view of the apparatus used by Stenzel and Gekelman to study magnetic reconnection. Current is pulsed through plates 30 cm apart is order to initiate reconnection. [18]. (b) Detailed side view of the apparatus [19]. Plasma is produced by continuously pulsing a bias between the cathode and nearby anode. Coils around the vacuum chamber create a uniform B-field in the axial direction.

The experiment relied on the reproducibility of the plasma and reconnection event. The experiment could be run once a second and a single probe was moved after each shot in order to measure the magnetic field at different locations. The measurements at a single location were averaged over multiple shots in order to ensure the data described the average reconnection event.

The most significant finding of this experiment is that the width of the reconnection layer is a few electron inertial lengths, c/ω_{pe} [18, 20]. They also found that the plasma flowing out of the reconnection layer was flowing at the Alfvén speed as predicted by the Parker model [20].

3.2 TS-3

The TS-3 device studied magnetic reconnection at the University of Tokyo in the 1990s [21]. The reconnection observed in this device is different from the UCLA reconnection experiment in several ways. Functionally, TS-3 merges two spheromaks to initiate magnetic reconnection instead of initiating magnetic reconnection

by forcing flux through the plasma as was done in the UCLA device. A schematic of TS-3 is shown in Figure 8a. In TS-3, the ion gyroradii are much smaller than the size of the plasma, so the reconnection is fully in the MHD regime. This was not the case in the UCLA device. Instead of relying on the shot-to-shot reproducibility of the plasma to measure the magnetic field like the UCLA experiment, the magnetic field in TS-3 was measured using a probe array. This allows the TS-3 magnetic field measurements to capture shot specific intricacies that are lost when averaging measurements over multiple shots. The UCLA experiment ensured that a single component of the magnetic field was small in order to create a 2D scenario, one of the conditions under which the Parker model is valid. The magnetic field in the TS-3 experiments had significant components in all 3 orthogonal directions. They are not 3D reconnection experiments, however, because the spheromaks have azimuthal symmetry.

The TS-3 device is capable of studying the merging of spheromaks with the same or opposite magnetic helicities. The former scenario is called co-helicity merging while the latter scenario is called counter helicity merging. Many experiments at TS-3 focus on the difference between co- and counter-helicity merging. Typical plasma parameters in TS-3 are $n = 3 \times 10^{14}$ cm^{-3}, $T_e = 5 - 15$ eV and toroidal magnetic field $B_\phi = 1$ kG. The experiments found that counter-helicity merging results in a higher reconnection rate than co-helicity merging. They also found that the reconnection rate is proportional to the inflow speed of the spheromaks [21]. Later TS-3 experiments observed ion heating and acceleration [22]. Figure 8b shows one instance of ion heating as a result of reconnection in TS-3.

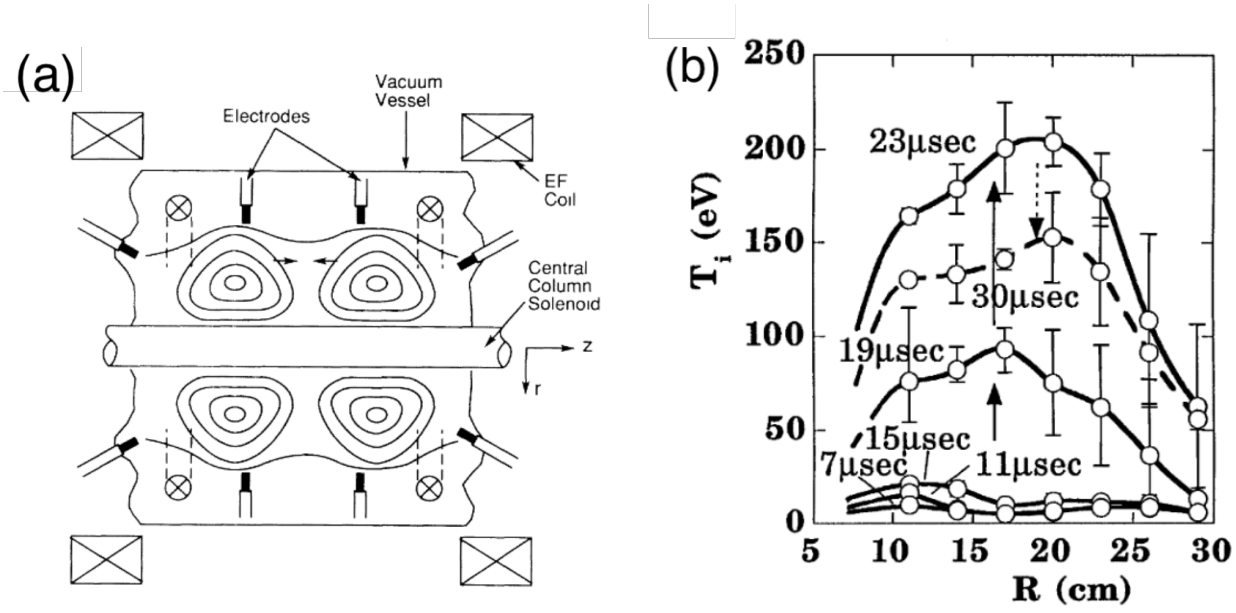

Figure 8: (a) A schematic of the TS-3 device [21]. (b) Observed ion heating in TS-3 [22].

3.3 MRX

The MRX device at the Priceton Plasma Physics Laboratroy studied magnetic reconnection starting in the late 1990s. The device, shown in Figure 9, consists of a cylindrical conducting shell with two conducting "flux cores" inside the chamber. Current is passed through the flux cores and varied in order to generate plasma and then subsequently initiate reconnection. The magnetic structure of the reconnection was measured with a probe array placed on an r-z plane. Other diagnostics include Langmuir probes for measuring electron density and temperature. The plasma in MRX is in the MHD regime. Typical plasma parameters are $B = 0.3 - 0.6$ kG, $T_e = 10 - 30$ eV, and $n_e = 0.5 - 2 \times 10^{14}$ cm^{-3} [23].

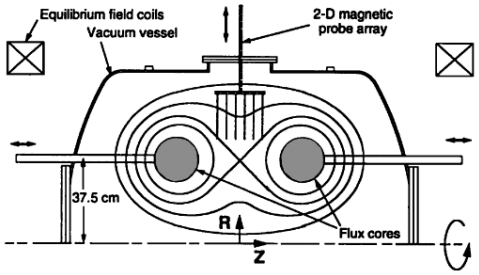

Figure 9: A schematic of the MRX device [23].

The MRX experiments revealed the presence of a double-Y shaped reconnection layer during null helicity reconnection just as predicted by the Parker model. An O-shaped reconnection layer was observed during co-helicity reconnection [23]. The Y and O shaped reconnection layers observed are shown in Figure 10. The reconnection rates observed at MRX were compared to those predicted by the Sweet-Parker model. The Parker model failed to account for the observed reconnection rates. However, a modified Parker model that accounts for the compressibility of the plasma and treats plasma pressure differently than the traditional Parker model is able to explain the observed reconnection rates [24]. A comparison of the observed reconnection rates to the modified and unmodified Parker model is shown in Figure 11.

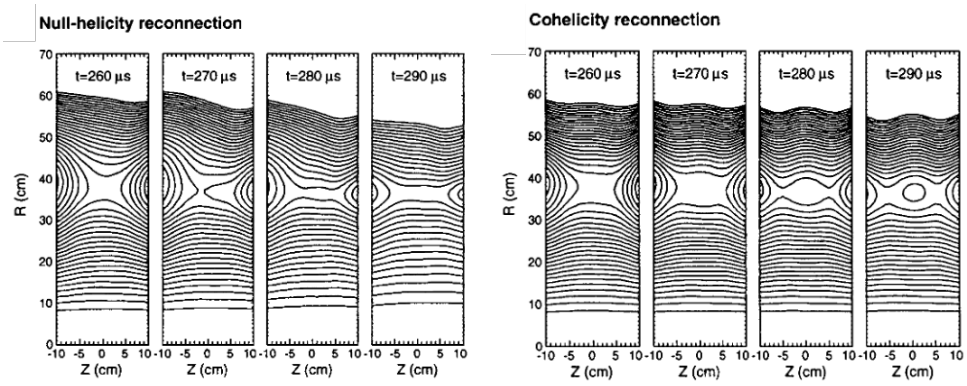

Figure 10: Comparison of null and co-helicity reconnection in MRX. Null helicity results in a double-Y shaped reconnection layer while co-helicity results in an O-shaped reconnection region [23].

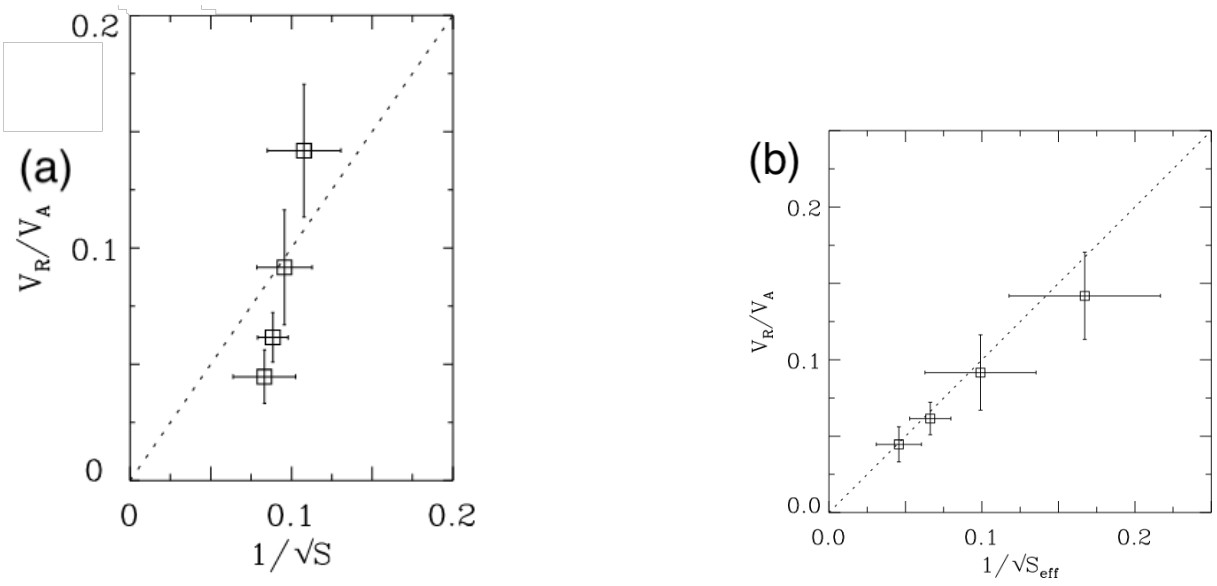

Figure 11: (a) Observed reconnection rates in MRX as compared with the Sweet-Parker model [24]. (b) Observed reconnection rates in MRX as compared with a modified Sweet-Parker model. The modified model takes into account the compressibility of the plasma and treats the role of plasma pressure in reconnection differently than the standard Parker model [24].

3.4 Early SSX Experiments

The SSX device was initially set up as shown in Figure 12 to perform 2D magnetic reconnection experiments. This was done by merging axisymmetric spheromaks. Spheromak plasmas were produced on either end of the device with magnetized plasma guns. The guns accelerate the spheromaks towards the middle of the device where they merge and undergo magnetic reconnection. Just like TS-3 and MRX, SSX has the ability to study co-helicity and counter-helicity merging configurations. Typical plasma paramters are $T_e = 20$ eV and $n_e = 10^{14}$ cm^{-3} [4].

An O-shaped reconnection layer, shown in Figure 13, was observed during counter-helicity merging of spheromaks at SSX [10]. Since the MRX experiments observed an O-shaped reconnection layer during co-helicity experiments, it has been shown that the shape of the reconnection layer is not simply a function of the initial helicity of the reconnection scenario. The thickness of the reconnection layer was observed to be c/ω_{pi}. The axisymmetric SSX experiments also found a energetic ion flux emanating from the reconnection layer. The ion flux was observed to peak 5 μs after the magnetic peak at a distance 50 cm from the reconnection layer indicating an outflow speed of 10^7 cm/s, the Alfvén speed [4].

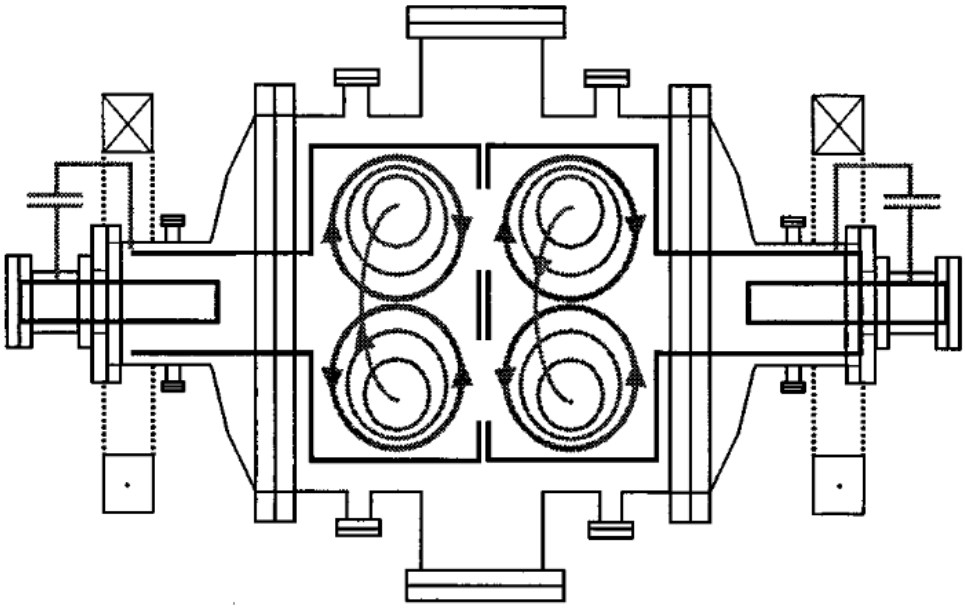

Figure 12: A schematic of the SSX device as set up to study axisymmetric spheromak merging. Magnetized plasma guns generate fully ionized plasma at either end of the device and accelerate the plasma towards the center where merging occurs. [4]

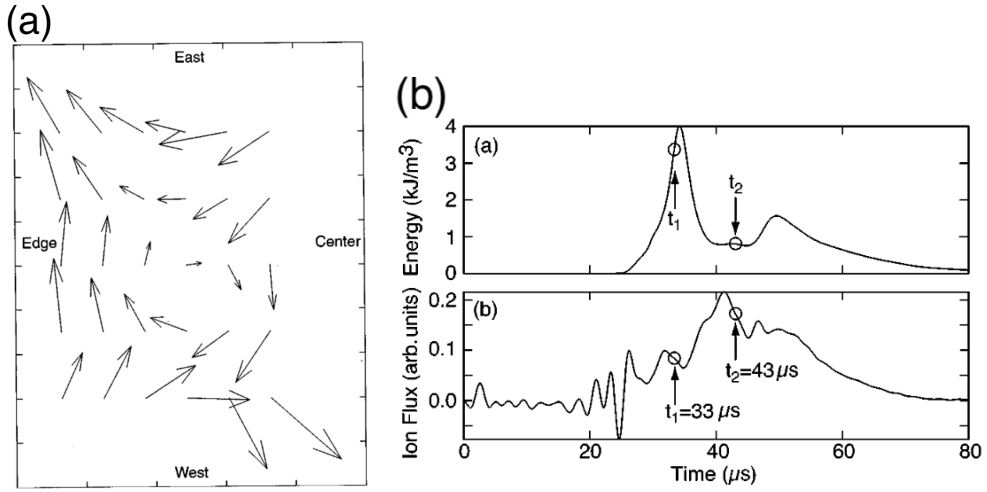

Figure 13: (a) Observed o-shaped reconnection layer during counter helicity merging at SSX [10]. (b) Magnetic energy peak followed by a 5 μs delayed observation of ions 50 cm from the reconnection region at SSX indicates Alfvénic ion outflows [4].

4 Experiment and Device Setup

Nearly all prior laboratory studies of magnetic reconnection have been 2D in that the reconnection geometry does not vary along one coordinate. We have performed a laboratory study of 3D magnetic reconnection by using a new iteration of the Swarthmore Spheromak Experiment (SSX) device to merge Taylor states. A schematic of the SSX device is shown in Figure 14. Before plasma is produced, the SSX vacuum chamber is evacuated to 10^{-7} Torr. This allows hot plasma to enter the chamber without being cooled down by the room temperature air. Spheromak plasmas made from fully ionized hydrogen gas are produced using magnetized plasma guns at either end of the device. The spheromaks move towards each other down thick walled copper cylinders with inner radius $R = 7.8$ cm. As the spheromaks move, they relax into their lowest energy state, a Taylor state. At the center of SSX, the Taylor states become radially unconstrained and merge. The width of the merging region is 17.3 cm wide. Magnetic reconnection occurs due to the overlap of the magnetic field of each Taylor state. The evolution of spheromaks into Taylor states is governed by turbulence. This means that the angle at which the the magnetic field at the leading edge of the Taylor states merge varies from shot to shot.

We collected data on 604 instances of Taylor state merging. During each shot, the magnetic field inside the merging plasmas is measured in 16 different locations in an r-z plane as shown in Figures 14 and 15. The electron density along the center of the merging region is measured using Mach-Zehnder interferometry. The ion temperature is measured along a chord which goes through the center of the merging region using ion Doppler spectroscopy as shown in Figures 15 and 14. The relative positions of the diagnostics are shown in Figure 15. The next sections explain the workings of the plasma guns and each diagnostic.

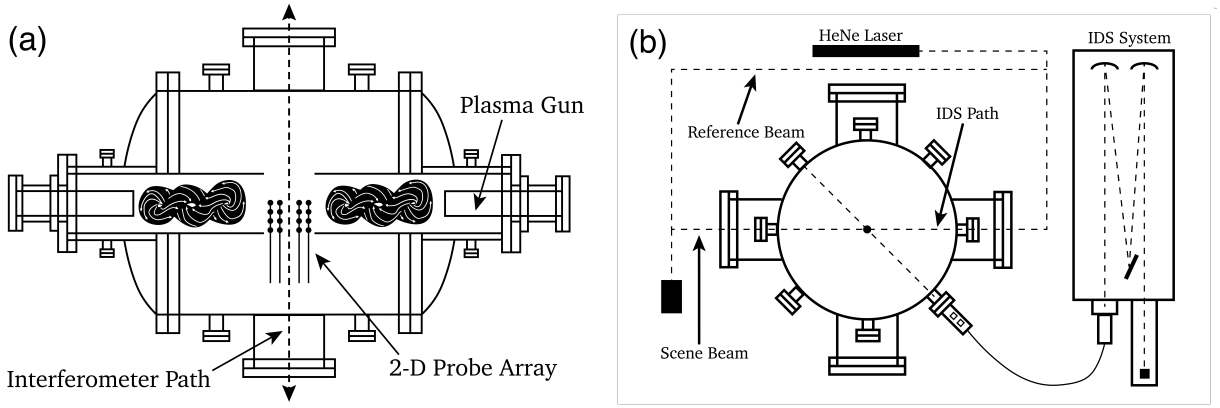

Figure 14: (a) An r-z cross sectional view of the SSX device. (b) An on-axis view of the SSX device. Spheromaks are produced on either side of the device using magnetized plasma guns. The spheromaks move through flux conservers towards the center of the device and evolve into Taylor states. The Taylor states merge in the center of the device uncontrained by flux conservers. The merging is studied using a magnetic probe array, Mach-Zehnder interferometery, and ion Doppler spectroscopy.

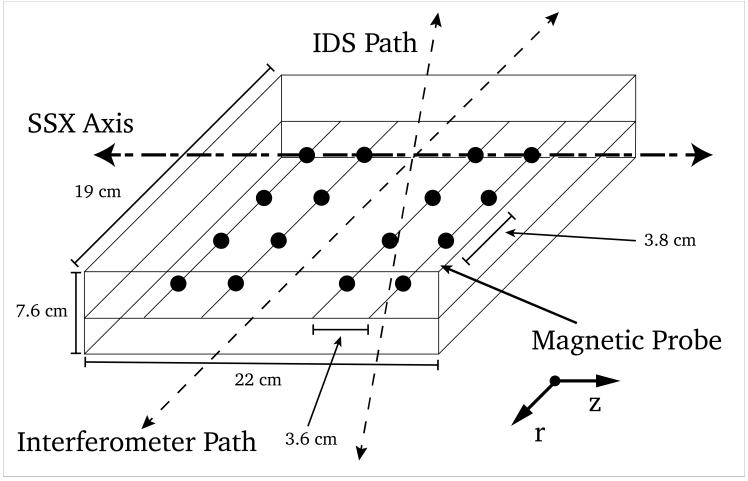

Figure 15: The relative positions of each diagnostic. The interferometer passes through the center of SSX. The IDS telescope is positioned to observe light along a diameter that goes through the center of SSX. The magnetics probes are arranged in a 4 x 4 grid on one side of the axis of SSX. Magnetics measurements

4.1 Plasma Production

SSX produces plasma using cylindrical magnetized plasma guns. Each gun consists of a coaxial solid cylindrical inner electrode and a cylindrical shell outer electrode. The space between the inner and outer electrode begins as a vacuum. A small amount of H_2 gas is puffed into the area between the inner and outer electrode of the gun and a current is passed through an external coil to create a poloidal magnetic field called the stuffing field as shown in Figure 16a. When the gas fills the entire area between the electrodes, the inner electrode is biased at -4 kV relative to the outer shell using a 1 mF capacitor. This is shown in Figure 16b. The strong electric field between the electrodes ionizes the hydrogen atoms in the gas which breaks the H_2 bond and turns the gas into a hydrogen plasma consisting of protons and free electrons. Now that there is a conducting plasma between the electrodes rather than a neutral gas, current flows through the plasma and down the inner electrode. The current flowing down the inner electrode makes a toroidal magnetic field which is embedded in the plasma. A $\mathbf{J} \times \mathbf{B}$ force pushes the plasma out of the gun as in Figure 16c. As the plasma moves out of the gun past the stuffing field, the stuffing field is embedded in the plasma as a poloidal field. Finally, the formed spheromak exits the gun with its embedded toroidal and poloidal fields as in Figure 16d.

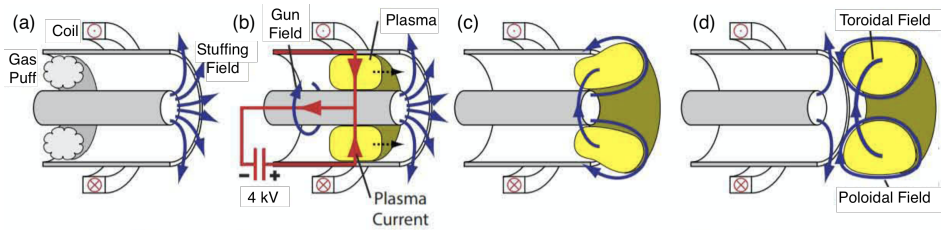

Figure 16: Formation of a spheromak using a coaxial plasma gun. (a) Gas is puffed between the inner and outer electrodes. External coil creates a poloidal magnetic field. (b) A capacitor biases the inner electrode at -4 kV and ionizes the gas. Current flows down the inner electrode and generates a toroidal field. (c) A $\mathbf{J} \times \mathbf{B}$ force pushes the plasma out of the gun. (d) The spheromak exits the gun with an embedded toroidal and poloidal field. [25]

4.2 B-dot Probe Array

The magnetic field inside the plasma is measured by a planar 4×4 array of B-dot probes. Each probe consists of three mutually perpendicular loops of wire whose ends extend out of SSX so the voltage around the coil can be measured by high speed data acquisition modules. The data acquisition units were configured to sample at 32 MHz for 125 μs. Each coil measures the component of the magnetic field at the probe's location perpendicular to its area. Each of the three coils is wound around a delrin rod to hold it in place. The probes and delrin rods are surrounded by quartz tubes to protect them from the plasma. A schematic of the probe array in SSX is shown in Figure 15. The axial probe spacing is 3.6 cm and the radial probe spacing is 3.8 cm. The probe array therefore does not allow for the determination of the exact magnetic structure of the reconnection. It does, however, allow for the determination of the magnetic energy in a 22 x 19 x 7.6 cm box delimited by the probes.

The magnetic field perpendicular to each coil is measured using Faraday's law. According to Faraday's Law,

$$V = -N\frac{d}{dt}\int_A B_\perp(t)\cdot dA \tag{4.1}$$

where $B_\perp$ is the component of the magnetic field that is perpendicular to the coil, N is the number of turns, and A is the cross sectional area of the coil. We can simplify Faraday's law to $V = -N\frac{d}{dt}(B_{\perp,av}A)$ or

$$B_{\perp,av}(t) = B_{\perp,av}(0) - \frac{1}{NA}\int_0^t V(t)dt \tag{4.2}$$

where $B_{\perp,av}$ is the average magnetic field over the area of the probe that is perpendicular to its cross section. Since B at an infinitesimally small point is impossible to measure with a finite area coil, the value of B_{av} is assigned to B at the center of the coil. In this way, the B-dot probe array allows for the measurement of the magnetic field at 16 locations inside the plasma.

4.3 Interferometer

The electron density is SSX is measured using a modified Mach-Zehnder interferometer. A complete explanation of the SSX interferometer can be found in Tim Gray's thesis [26]. A 632.8 nm HeNe laser is split by a beam splitter to produce two beams which traverse two equal length paths. One beam, the scene beam, travels through the plasma. The other beam, the reference beam, travels through air. The reference beam is circularly polarized using a $\lambda/4$ waveplate. The beams are recombined after traversing their paths and then split by a Wollaston prism into components polarized parallel and perpendicular to the prism's optical axis. The presence of plasma in the path of the scene beam rotates the polarization of the recombined beam counterclockwise. Measurement of the intensity of both components of the recombined beam allows for the determination of the phase shift of the light caused by the plasma. The shift in the phase of the recombined beam is related to the line averaged plasma density by

$$\Delta\phi = \frac{\lambda e^2}{4\pi c^2 \epsilon_0 m_e}\int_{\Delta z} n(z)\ dz \tag{4.3}$$

where λ is the wavelength of the laser, e is the elementary charge, and Δz is the distance in the path of the scene beam that contains plasma [7]. Thus, the interferometer allows for the measurement of the line

average plasma density $\frac{1}{\Delta z}\int_{\Delta z} n(z)\, dz$.

4.4 Ion Doppler Spectrometer

SSX plasmas are pure hydrogen plasmas, but they contain trace amounts of impurities such as carbon. These impurities are present, because the the hydrogen gas puffed into SSX to create the plasma is not 100% pure. Atoms other than hydrogen are also scraped off the walls of SSX by the hot plasma. At SSX temperatures, 2 electrons are stripped from carbon atoms to form doubly ionized carbon ions which are denoted C_{III}. The bound electrons in C_{III} move between energy levels due to the heat of the plasma and emit light which is Doppler shifted according to the ion velocities. The SSX ion Doppler spectrometer determines the proton temperature by measuring the broadening of the 229.687 nm line in C_{III}.

The SSX ion Doppler spectrometer uses an optical fiber to collect light from the plasma along a chord which passes through the center of the merging region [27]. The collected light is fed into a McPhearson Model 209 monochromator which filters out all wavelengths other than the Doppler broadened 229.687 nm C_{III} line of interest and then spreads the light out onto an array of photomultiplier tubes, PMTs, using a 25^{th} order echelle grating. Each PMT in the array measures the intensity of 229.687 nm light with a specific Doppler shift. The signals from each PMT over time thus allows for the measurement of the velocity distribution of the carbon ions along the line of sight of the optical fiber. For an MHD plasma, particles have a Maxwellian velocity distribution which means that the 1D velocity distribution function that is measured by the IDS system is a 1D Maxwellian distribution

$$f(v) = n\left(\frac{m}{2\pi kT}\right)^{1/2} \exp\left(\frac{-m(v-v_0)^2}{2kT}\right) \tag{4.4}$$

where m is the mass of a C_{III} ion, n is the average impurity ion density, v_0 is the mean velocity of ions towards or away from the optical fiber, and T is the temperature of the C_{III} ions [28]. Wider velocity distributions correspond to larger temperatures and narrower distributions correspond to lower temperatures.

The carbon ions equilibrate with the protons on a timescale less than 0.5 μs, so the carbon ion temperature and proton temperature are equal on a timescale of 1 μs [27]. The IDS system thus determines the proton temperature every microsecond. A sample fit of a Maxwellian to a velocity distribution to yield a temperature measurement is shown in Figure 17. Since the fit is made to a plot of photon count vs velocity instead of impurity count vs velocity, the fit function is

$$\text{Photon count} = I_0 \exp\left(\frac{-m(v-v_0)^2}{2kT}\right) \tag{4.5}$$

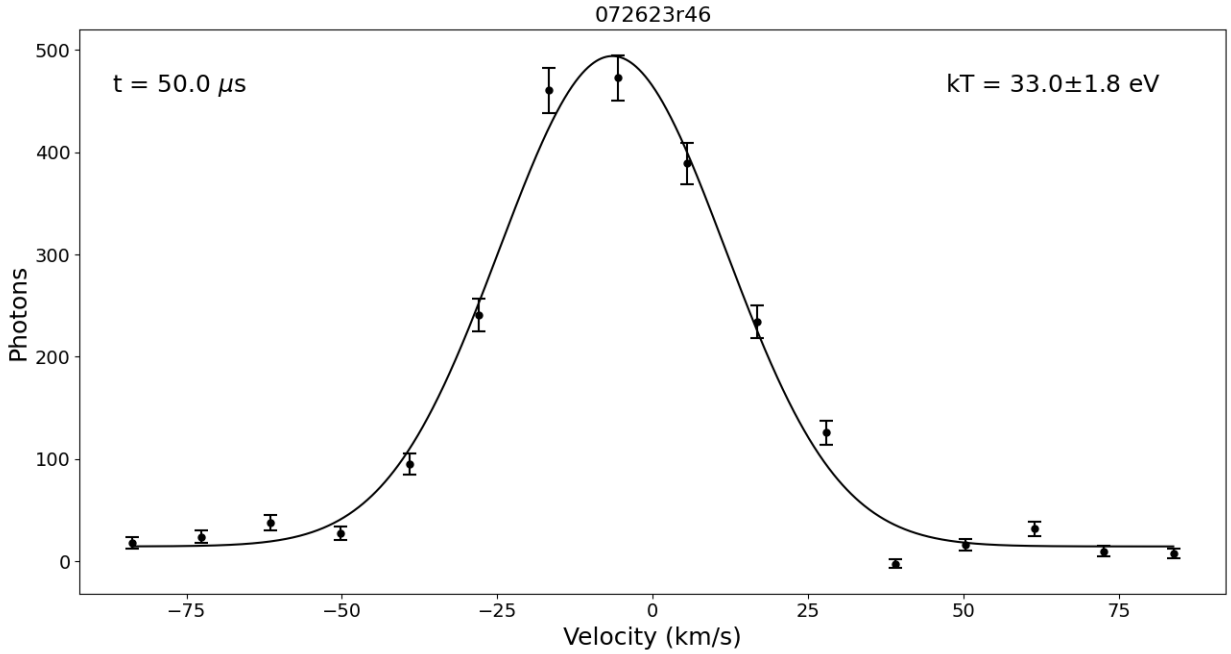

Figure 17: A Maxwellian fit to a velocity distribution measured by the SSX IDS system from observation of the Doppler shift of the C_{III} 229.67 nm line. The distribution is of the form photon count $= I_0 \exp\left(\frac{-m(v-v_0)^2}{2kT}\right)$.

5 Results and Discussion

We took 604 shots of Taylor state merging using the SSX device. 354 shots merged Taylor states of the same magnetic helicity, co-helicity merging. 251 shots merged Taylor states of opposite magnetic helicity, counter helicity merging. All of the shots were performed with 4.0 kV on the capacitor banks and and stuffing flux of $\Phi_{gun} = 1.0$ mWb. During each shot, we measured the line-averaged electron density with Mach-Zehnder interferometry, line averaged ion temperature with ion Doppler spectroscopy, and the magnetic field at 16 different locations with a probe array as detailed in section 4. The magnetic field was used to calculate the magnetic energy in the box delimited by the probe array.

5.1 Typical Shots

Data from a typical shot is shown in Figure 18. Measurements start around 28 μs, when the Taylor states reach the diagnostics at the center of SSX and begin to merge. Merging ends around 95 μs. The density, ion temperature, and magnetic energy oscillate over the course of the shot with multiple prominent peaks. Oscillations in all three quantities were observed in all shots, but the number of peaks and peak locations in each of the density, ion temperature, and magnetic energy varies from shot to shot. The merging of Taylor states is not a steady state process as in the Parker model. Since all measurements are made in fixed locations, we cannot distinguish between spatial and temporal variations. The periodic structure of the twisted magnetic flux ropes may be related to the periodic nature of the merging, especially the magnetic energy oscillations, but the details of its role is unclear. Figure 18 shows that the density reaches its maximum early in the merging and the temperature reaches its maximum later. A previous study of Taylor state merging at SSX by Gelber and Brown with identical experimental parameters and diagnostics as this study found a density peak followed by a later temperature peak when averaging over multiple shots [29]. When averaged over multiple shots, electron density and ion temperature displayed no oscillations [29]. We have seen density, ion temperature and, magnetic field oscillations in every shot which were not noted in the previous study by Brown and Gelber. We have also found electron density and ion temperature peaks that are of similar magnitude to the maximum electron density and ion temperature which may be just as important to the merging as the initial density maximum and subsequent temperature maximum observed by Brown and Gelber when averaging over multiple shots [29].

Measurement of the magnetic field in the plane of the probe array allows for the calculation of current density in the same plane via Ampère's law. The displacement current was considered negligible as in the MHD Ampère's law, because Taylor states are MHD plasmas. We visualized the magnetic field and current density in the plane of the probe array by creating movies of moving arrows overlaid on a variable heat map. The magnetic field and current of different shots look very different from one another. No two shots look alike. This is most likely due to the shot-to-shot variation in the merging angle between the magnetic field at the leading edge of the Taylor states. Within a single shot, the magnetic field greatly varies in both magnitude and direction. This leads to the formation of irregular current shapes. A typical observed current density is 5×10^6 A/m^2. Figure 19 shows the current density at four times in the same shot. The times chosen were selected at magnetic energy peaks in order to show the largest observed current densities. At $t = 39.25000$ μs we see an inner and outer current sheet which face in opposite directions. At $t = 57.46875$ μs nearly the entire current sheet points the same direction. At $t = 30.78125$ μs and $t = 48.34375$ μs the current sheet has no clear structure. The limited size of our probe array prevents us from making detailed comments about the current in merging Taylor states, but we can clearly see that Taylor state merging produces complex

current geometries. This is unlike the magnetic reconnection of axisymmetric spheromaks which produces a single current sheet.

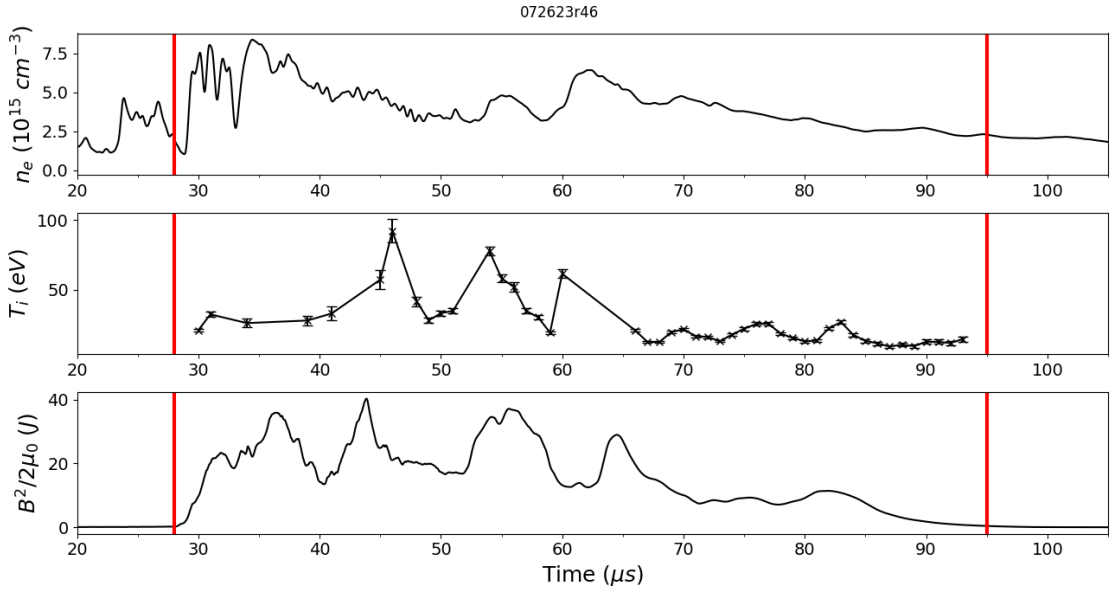

Figure 18: Electron density, ion temperature, and magnetic energy for a typical shot. Electron density and ion temperature are measured along cords going through the SSX midplane. Magnetic energy is calculated in the box delimited by the probe array. The merging epoch is 28 – 95 μs.

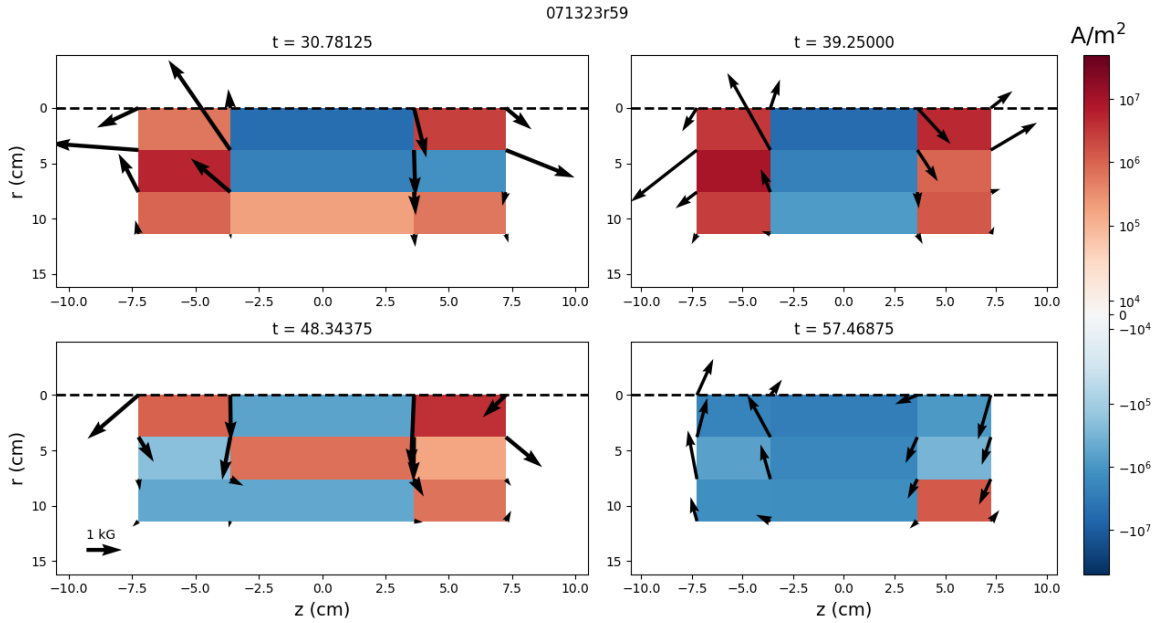

Figure 19: The average current density in the space between the probes at four different times corresponding to magnetic energy peaks. At $t = 39.25000$ μs the current sheet reverses direction at the SSX midplane. At $t = 57.46875$ μs the current almost completely points in a constant direction. At $t = 30.78125$ μs and $t = 48.34375$ μs there is no clear pattern in the current.

5.2 Summary Statistics and Correlations

Our diagnostics are too limited to determine the magnetic, density, or temperature geometries produced by Taylor state merging. They are, however, sufficient for calculating quantities which summarize each shot. We call these quantities summary statistics for ease of reference. For each shot, we calculated the average and peak values of electron density, ion temperature, and magnetic energy during the merging epoch $28 - 95$ μs. Average values are denoted with a bar. These values were used to calculate $\overline{v_A} = \overline{B}/\sqrt{\mu_0 \overline{n_e}}$, $\overline{t_A} = R/\overline{v_A}$, $\overline{\rho_i} = \overline{T_i}^{1/2} m_p^{1/2}/e\overline{B}$, and $\overline{\beta_i} = 2\mu_0 n \overline{T_i}/\overline{B}^2$, all averages. $\overline{B}$ is the average magnetic field on the axis of SSX where it is strongest, m_p is the mass of a proton, e is the elementary charge, and $R = 7.8$ cm is the inner radius of the flux conserver. We also calculated the time between the maximum density and maximum ion temperature which we call heating time. A positive heating time means density reached its maximum before ion temperature. A negative heating time means ion temperature reached its maximum before density. Figures 20 and 21 show the distributions of each summary statistic. The mean of each summary statistic is shown in Table 1.

We would like to examine the shape of the distribution of each summary statistic, but due to the lack of theoretical predictions for 3D magnetic reconnection or Taylor state merging, we don't know what distributions to expect. We compared the distribution of each summary statistic to a normal distribution using a Q-Q plot. The normal distribution was chosen due to its special role in the central limit theorem, and because many of the distributions we measured looked similar to a normal distribution. It should be acknowledged, though, that there is no theoretical basis for comparing each distribution to a normal distribution. The $\overline{n_e}$ distribution has a heavier right tail and a lighter left tail than a normal distribution. The distribution of peak W_{mag} is approximately normal but with heavier tails. The $\overline{T_i}$ and peak n_e distributions match the normal distribution near the median and on right tail. They deviate from normality in the left tail. This deviation from normality is much more pronounced in peak n_e than in $\overline{T_i}$. The distribution of $\overline{T_i}$ is the closest to a normal distribution of any of the summary statistics. Both $\overline{W_{mag}}$ and $\overline{v_A}$ are skewed left. Peak T_i, $\overline{t_A}$, $\overline{\beta_i}$, and $\overline{\rho_i}$ are all skewed right. The Q-Q plot for heating time is particularly interesting. It shows strong agreement with a normal distribution around the median and to the right of the median. To the left of the median, particularly at negative heating times less than -10 μs, the distribution of heating times deviates from a normal distribution. There is not enough theory on 3D magnetic reconnection to comment on the meaning of the distribution shapes.

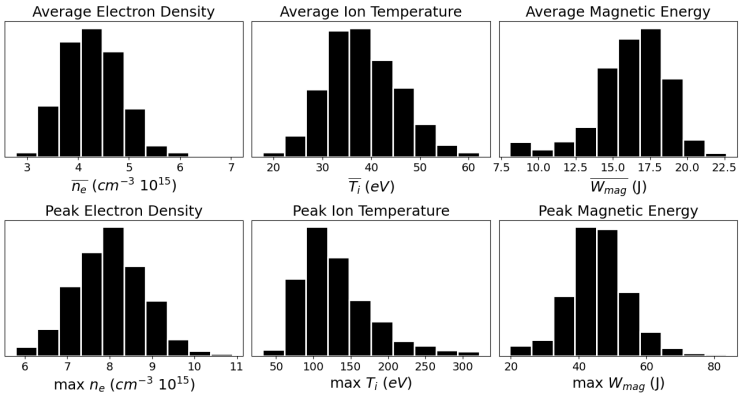

Figure 20: Distributions for average (above) and peak (below) n_e, T_i, W_{mag}.

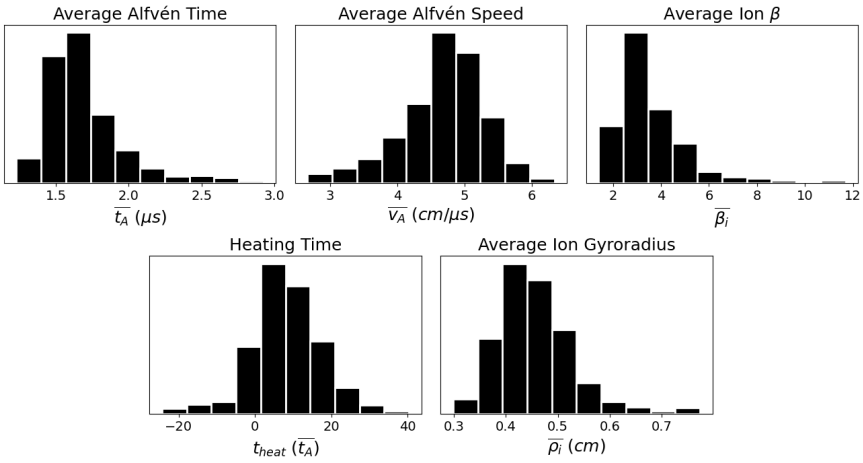

Figure 21: Distributions for average t_A, v_A, β, ρ_i, and heating time.

	Overall	Co-helicity	Counter-helicity
$\overline{n_e}$ (cm^{-3} 10^{15})	4.28 ± 0.02	4.18 ± 0.03	4.43 ± 0.04
$\overline{T_i}$ (eV)	38.3 ± 0.4	37.2 ± 0.4	39.9 ± 0.4
$\overline{W_{mag}}$ (J)	16.2 ± 0.1	17.1 ± 0.1	15.0 ± 0.2
peak n_e (cm^{-3} 10^{15})	8.00 ± 0.03	7.90 ± 0.05	8.14 ± 0.05
peak T_i (eV)	131 ± 2	124 ± 2	141 ± 3
peak W_{mag} (J)	45.8 ± 0.4	48.2 ± 0.4	42.6 ± 0.6
$\overline{\beta_i}$	3.59 ± 0.06	3.15 ± 0.05	4.2 ± 0.1
$\overline{v_A}$ ($\mathrm{cm}/\mu s$)	4.68 ± 0.03	4.83 ± 0.02	4.48 ± 0.05
$\overline{t_A}$ (μs)	1.70 ± 0.01	1.630 ± 0.008	1.80 ± 0.02
$\overline{\rho_i}$ (cm)	0.457 ± 0.003	0.438 ± 0.003	0.483 ± 0.005
Heating time ($\overline{t_A}$)	8.3 ± 0.4	8.2 ± 0.5	8.3 ± 0.6

Table 1: Mean of each statistic across all shots, during co-helicity merging, and during counter-helicity merging.

Most shots display a positive heating time, but 14.6% of the total shots have a negative heating time. This is true for 13.8% of the co-helicity shots and 15.6% of counter-helicity shots. Data from a shot with a negative heating time is shown in Figure 22. While the maximum temperature does occur before the maximum density, the shot displays an initial density pulse followed by a heating pulse as well as oscillatory behavior just like the shots with positive heating times. The maximum density and maximum temperature may be related. This would make the time between these peaks a key parameter for describing Taylor state merging. However, due to the episodic nature of the merging and the similar magnitude of the various density and temperature peaks that occur over the course of each shot, it is possible that the maximum density and temperature are not any more noteworthy than the other peaks. In this case, the process of Taylor state merging should be thought of as a series of density and temperature peaks rather than a single important peak in each quantity.

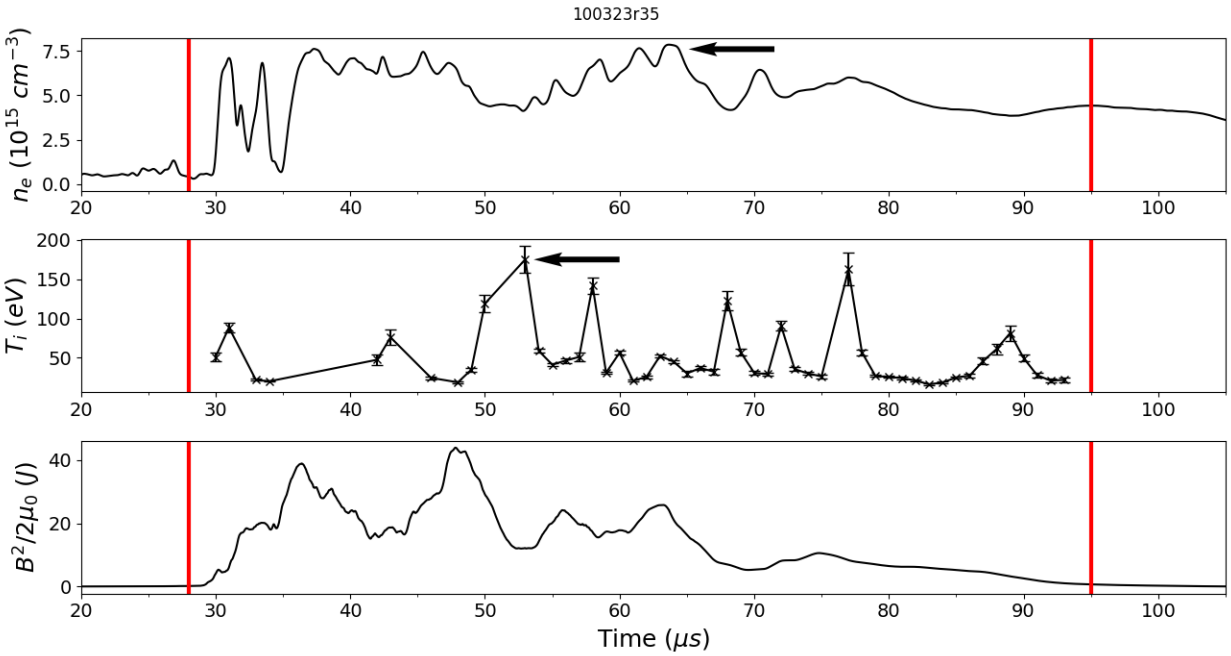

Figure 22: Electron density, ion temperature, and magnetic energy for a shot with where ion temperature reaches its maximum before electron density. Arrows point to the maximum values of electron density and ion temperature. Electron density and ion temperature are measured along cords going through the SSX midplane. Magnetic energy is calculated in the box delimited by the probe array. The merging epoch is 28 – 95 μs.

As shown in Figure 23a, we find a significant negative correlation between heating time and average Alfvén time among shots with positive heating times ($p < 0.01$). Figure 23c shows no significant correlation between heating time and average Alfvén time among shots with negative heating times ($p = 0.62$). The significant negative correlation among shots with positive heating times goes against our intuition about the relationship between heating time and Alfvén time. As the Alfvén time increases, we would expect heating time to increase due to the longer characteristic time for the merging, but the correlation we find is negative. If the maximum density and temperature are not more important in describing Taylor state merging than any other peaks, we would find no correlation between heating time and average Alfvén time. We do not understand why we observe this negative correlation.

The absence of a correlation among the shots with negative heating times may be due to insufficient data to reveal the correlation. As stated earlier, only 14.6% of the total shots, 88 shots, have a negative heating time. The lack of a correlation could also be due to the inability of heating time, the time between the maximum density and maximum temperature, to characterize Taylor state merging. As seen in Figure 18, there are multiple density and temperature peaks in each shot and, as stated earlier, the maximums may not be of particular importance.

Figure 23b shows a significant negative correlation between heating time and average ion gyroradius among shots with positive heating times ($p < 0.01$). Just as with Alfvén times, Figure 23d shows that no significant correlation is observed among shots with negative heating times ($p = 0.06$). We know that both $\overline{t_A} \propto \frac{1}{\overline{B}}$ and $\overline{\rho_i} \propto \frac{1}{\overline{B}}$ where, as stated earlier, $\overline{B}$ is the average magnetic field during the merging epoch on the axis of SSX, were the magnetic field is strongest. Figure 24 reveals a positive correlation between heating time and $\overline{B}$. We know that when heating time is positive, shorter $\overline{t_A}$, shorter $\overline{\rho_i}$, and larger $\overline{B}$ lead to longer

heating times. But we don't know which of $\overline{t_A}$, $\overline{\rho_i}$, or $\overline{B}$ is directly responsible for the longer heating times, because they are all functions of each other. Regardless of whether heating time is directly related to $\overline{t_A}$, $\overline{\rho_i}$, or $\overline{B}$, we do not have a theoretical explanation for the relationship.

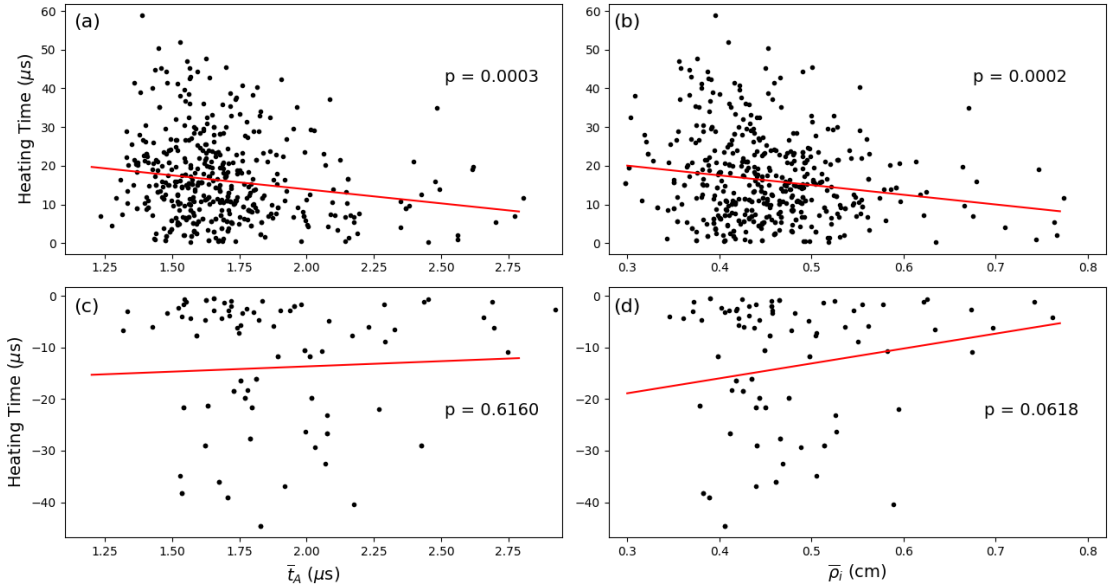

Figure 23: Heating time vs average Alfvén time for shots with positive heating times (a) and negative heating times (c). Heating time vs average ion gyroradius for shots with positive heating times (b) and negative heating times (d) Least-squares lines of best fit are shown. For shots with positive heating times, heating time and average Alfvén time as well as heating time and average ion gyroradius are negatively correlated ($p < 0.01$). Shots with negative heating times display no significant correlation between heating time and average Alfvén time or between heating time and average ion gyroradius ($p > 0.01$).

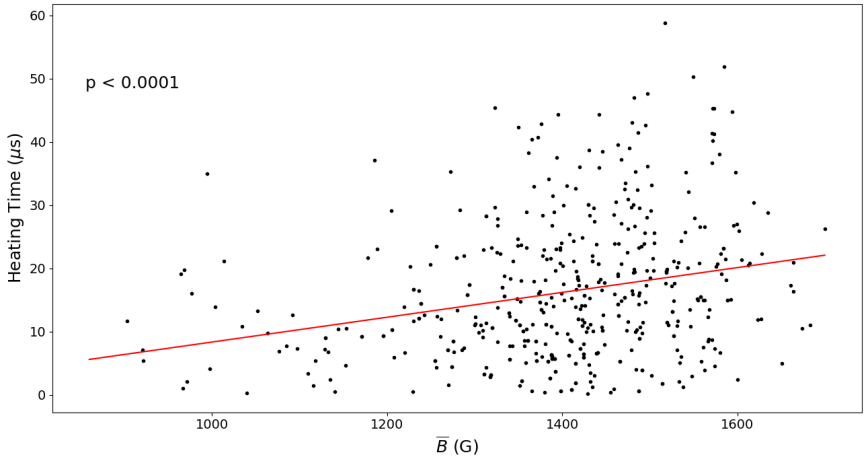

Figure 24: Heating time vs average magnetic field on the the axis of SSX for shots with positive heating times. The least-squares line of best fit is shown. Among shots with positive heating times, there is a significant positive correlation between the average magnetic field on the axis of SSX and the heating time ($p < 0.01$).

Table 1 shows that counter-helicity shots have higher mean values of average and peak ion temperature than co-helicity shots. One known affect of magnetic reconnection is ion heating, so we would expect the counter-helicity shots to also have higher mean values of average and peak magnetic energy [13]. However, average and peak magnetic energy have lower mean values in counter-helicity shots than in co-helicity shots. When examining all shots, both co and counter-helicity, we expect to see a positive correlation between one or multiple pairs of either average or peak ion temperature and average or peak magnetic energy due to the magnetic reconnection that occurs during Taylor state merging. Figure 25 shows scatter plots of average and peak ion temperature vs average and peak magnetic energy. The aggregate statistics examined do not reveal a correlation between magnetic energy and ion temperature. This suggests that the conversion of magnetic energy to heat during Taylor state merging is more complex than with 2D magnetic reconnection.

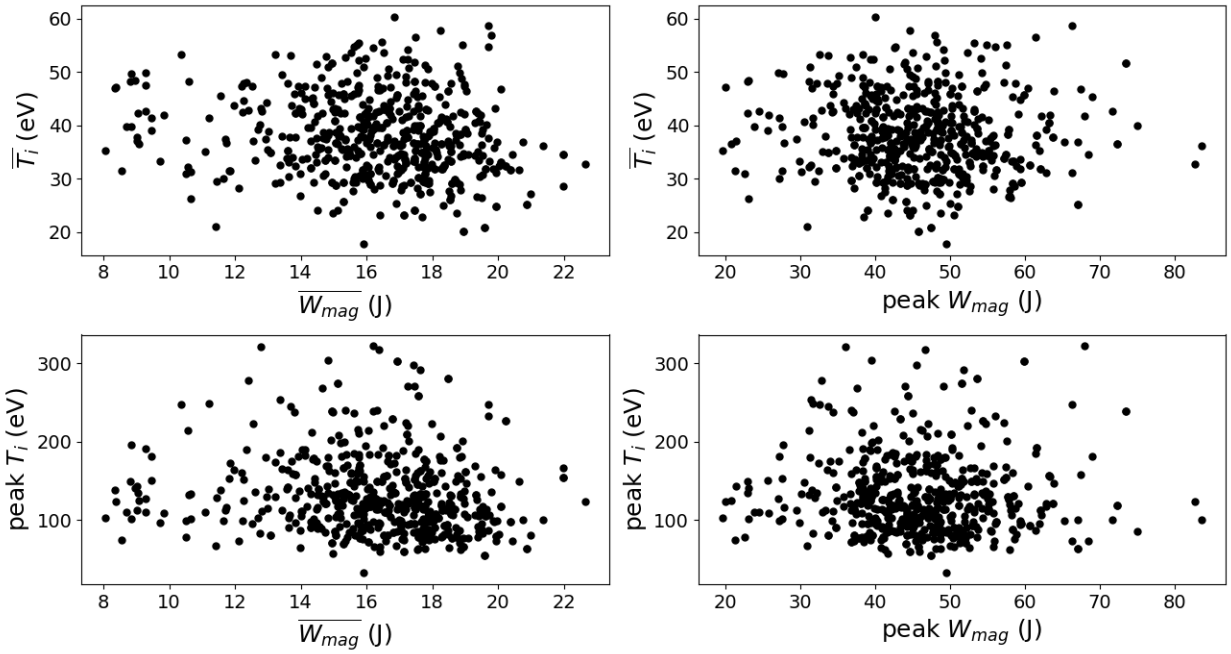

Figure 25: Average and peak T_i vs average and peak W_{mag} for the shot ensemble. There is no correlation between ion temperature and magnetic energy.

Counter helicity shots have higher mean values of average and peak density than co-helicity shots. Combined with higher ion temperatures and lower magnetic energy, ion dynamics in counter-helicity shots are on average more thermally dominated than in co-helicity shots. This is seen in the higher mean $\overline{\beta_i}$ among counter-helcity shots. Also noteworthy is that the mean heating times for both co and counter-helicty merging are about 8.3 $\overline{t_A}$. The heating time in units of Alfvén time is equal to the reciprocal of the Sweet-Parker reconnection rate if we assume that reconnection only occurs a single time during Taylor state merging. Accepting this assumption, we calculate a mean reconnection rate over the shot ensemble of 0.12, about 0.1, which has been observed in many other experiments and simulations [11].

5.3 Frequency Analysis

We can see in Figure 18 that the electron density, ion temperature, and magnetic energy all undergo oscillations over the course of merging. To explore these oscillations, we calculated the Fourier transform of each trace during the merging epoch 28 – 95 μs. A linear fit was subtracted from each trace in the merging epoch before taking tge Fourier transform to account for linear trends. For each shot, the frequency with the highest Fourier power above 40 kHz was recorded for the electron density, ion temperature, and magnetic energy. A cutoff frequency of 40 kHz was chosen, because low frequency modes below 40 kHz strongly dominate the Fourier transform of all traces. Figure 26 shows a histogram of these highest amplitude frequencies for the co-helicity shots, and Figure 27 shows a histogram for the counter-helicity shots. As frequency increases, all of the histograms display a decrease in counts which indicates the dominance of low frequencies. In both co and counter helicity shots, small peaks in magnetic energy and ion temperature are observed around 60 kHz. The counter-helicity shots display a peak in highest amplitude ion temperature frequency around 100 kHz. We also averaged the electron density, ion temperature, and magnetic energy traces in the frequency domain across all shots, the co-helicity, and the counter-helicity shots. This yields decreasing power spectra without any significant peaks. Many shots have electron density, ion temperature, or magnetic energy traces with highest amplitude Fourier modes above 40 kHz which suggests that oscillations are important to understanding unconfined Taylor state merging, but the exact nature of the oscillations has not been revealed. Advanced signal processing techniques such as wavelet transforms or more spatially resolute measurements of plasma parameters may be able to reveal the character of the oscillations.

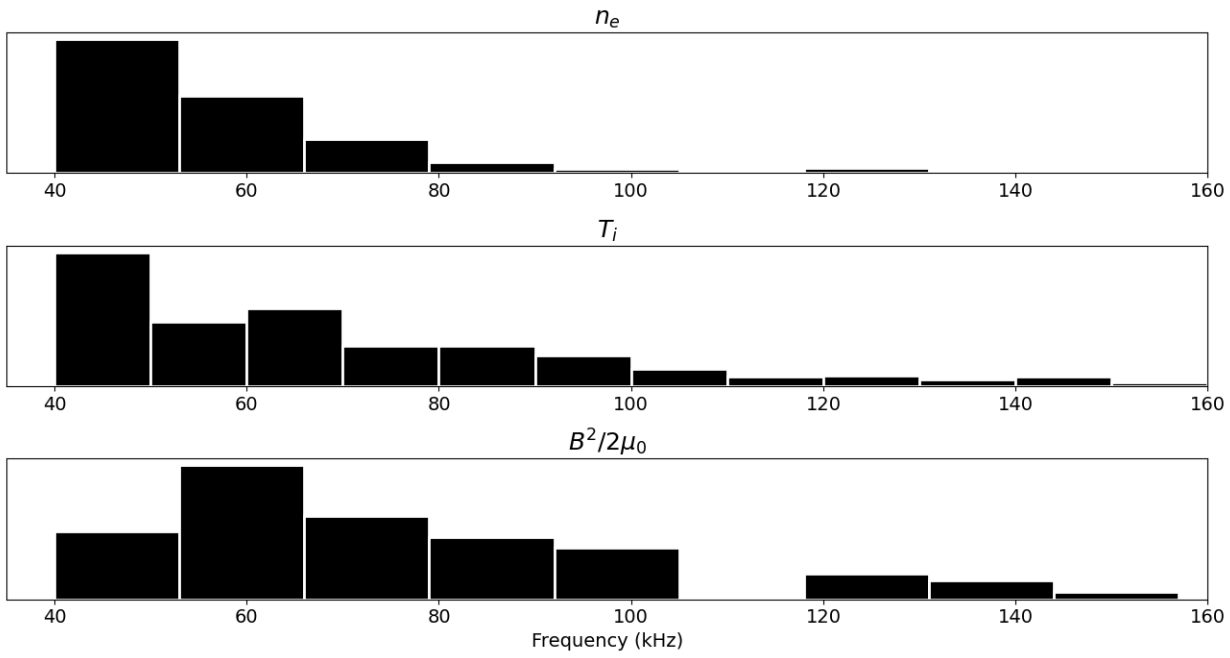

Figure 26: Histogram of highest amplitude Fourier mode for electron density, ion temperature, and magnetic energy in co-helicity shots. The ion temperature and magnetic energy traces have peaks around 60 kHz.

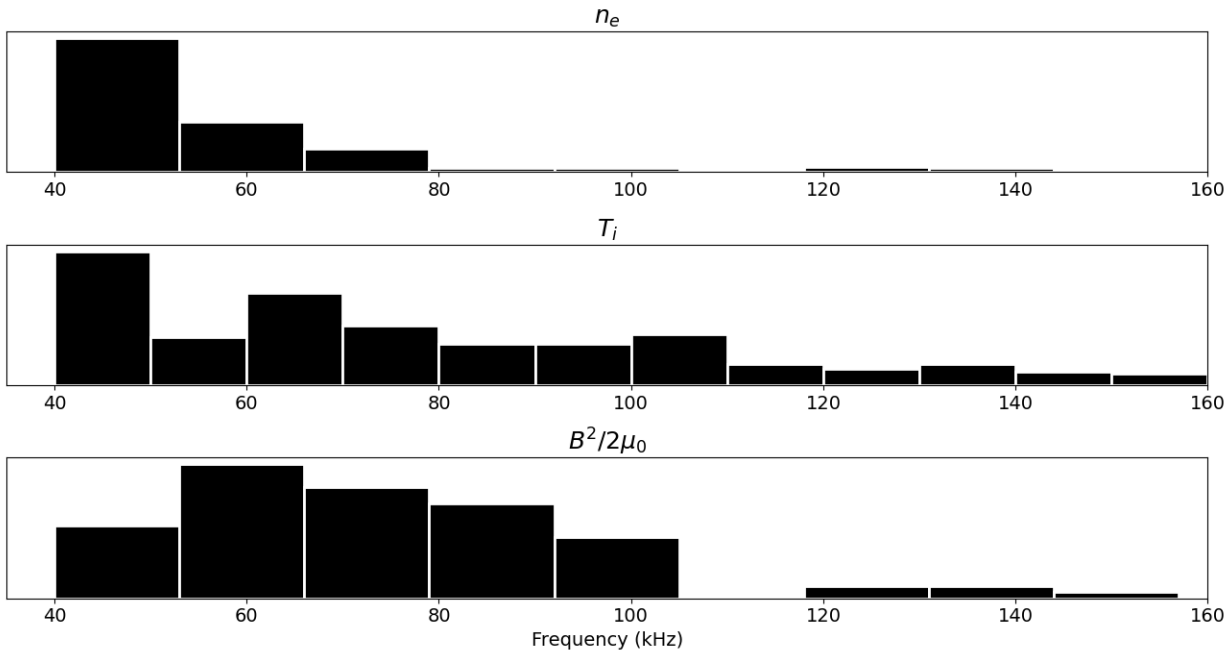

Figure 27: Histogram of highest amplitude Fourier mode for electron density, ion temperature, and magnetic energy in counter-helicity shots. The ion temperature and magnetic energy traces have peaks around 60 kHz. Ion temperature displayed an additional peak around 100 kHz.

6 Conclusion

This experiment is one of the first studies of 3D magnetic reconnection in laboratory plasmas. The merging of Taylor states is much more complex than 2D reconnection. The merging is dynamic rather than steady state like the 2D Sweet-Parker model. We have observed irregular magnetic field and current geometries which vary over the course of the merging. Electron density, ion temperature, and magnetic energy all oscillate over the course of the merging. The exact nature of the oscillations has not been revealed. Taylor state merging involves multiple prominent peaks in electron density, ion temperature, and magnetic energy. The maximum values of electron density and ion temperature are probably not especially important as was suggested by the previous SSX experiments by Brown and Gelber [29]. Analysis of the average and peak values of magnetic energy and ion temperature are unable to capture the conversion of magnetic energy to ion temperature via magnetic reconnection. Average Alfvén time and average ion gyroradius, both of which are inversely proportional to average magnetic field, are negatively correlated with heating time for shots with positive heating times. The theoretical basis for these correlations has not been determined.

7 Future Work

SSX will continue to study Taylor state merging in the summer of 2024. There are plans to perform a similar experiment to the one described in this thesis, but with the inclusion of electron temperature measurements. There is much work to be done studying 3D magnetic reconnection in laboratory plasmas. Future experiments could involve mapping out the magnetic field, density, ion temperature, and electron temperature at every point in a 3D reconnection geometry in a manner similar to Stenzel and Gekelman [18]. This would require a reproducible 3D reconnection event unlike the Taylor state merging described in this paper. Experiments could also look at the role of turbulence in magnetic reconnection.

8 Appendix A: Probe Array Details

8.1 Magnetic Probe Array Calibration Procedure

As stated in section 4.2, each B-dot probe consists of three mutually perpendicular loops of wire. We showed that the magnetic field perpendicular to a loop of wire can be calculated from the voltage around the loop.

$$B_{\perp,av}(t) = B_{\perp,av}(0) - \frac{1}{NA}\int_0^t V(t)dt \tag{8.1}$$

where A is the area of the loop and N is the number of turns.

One could measure the cross sectional area and record the number of turns in each of the three coils making up each single probe in order to solve for $\mathbf{B}$ in terms of the measured voltages on the probe. However, such a method would not account for the imperfections in probes construction. The three coils may not be perfectly perpendicular. It is also difficult to accurately measure the small cross sectional area of a single coil.

Instead of measuring N and A to be able to calculate B from the measured voltage on the probe, we use a different calibration mechanism for the probes. This process is detailed by Geddes, Kornack, and Brown [15]. Since the three coils making up each probe may not be perfectly perfectly perpendicular, we can say that $V_{x'}\hat{x}'+V_{y'}\hat{y}'+V_{z'}\hat{z}' = c_{x'}\dot{B}_{x'}\hat{x}'+c_{y'}\dot{B}_{y'}\hat{y}'+c_{z'}\dot{B}_{z'}\hat{z}'$ where $\hat{x}'$, $\hat{y}'$, and $\hat{z}'$ are linearly independent but not necessarily perpendicular unit vectors that point perpendicular to each of the 3 coils making up each probe. The value of the component of the magnetic field along each of the 3 orthogonal directions of a coordinate system is a linear combination of $B_{x'}\hat{x}'$, $B_{y'}\hat{y}'$, and $B_{z'}\hat{z}'$.

Three operations are required to solve for $\mathbf{B}$ at a single probe's location from the measured voltages. We must multiply the voltage on each of the three coils comprising the probe by the correct factor to find $\dot{\mathbf{B}}$. Then we must integrate $\dot{\mathbf{B}}$ to find $\mathbf{B}$ in the $\hat{x}'$, $\hat{y}'$, $\hat{z}'$ basis. Finally, we must perform a linear transformation on $B_{x'}\hat{x}'+B_{y'}\hat{y}'+B_{z'}\hat{z}'$ to find $\mathbf{B}$ in the orthogonal $\hat{x}$, $\hat{y}$, $\hat{z}$ coordinate system. These operations can be done in any order, because integration is a linear operation. To find $\mathbf{B}$, we first integrate the measured voltages $V_i(t),\ i = \ x',\ y',\ z'$ on each of the three coils that make up the probe to get $\mathbf{V}_{int}(t)$ then we multiply by the correct constants and transform the magnetic field into the $\hat{x}$, $\hat{y}$, $\hat{z}$ basis by the matrix multiplication

$$C\ \mathbf{V}_{int} = \mathbf{B} \tag{8.2}$$

where C is the calibration matrix for the probe which is calculated before the experiment.

The calibration matrix C is calculated for each probe via the following procedure. The probe array was placed inside a helmholtz coil with known dimensions, $R = 15.8$ cm and $N = 2$ turns per coil, such that the location of each probe is known. High current, about 10 kA, is pulsed through the coil and the voltages induced on each of the coils comprising each probe are recorded. The current through the helmholtz coil is measured using a Rogowoski coil. This process is done three times, each with the helmholtz coil pointing along a different directional axis of the coordinate system. On each of these so called calibration shots, a specific instant in time is selected to perform the calibration. At the chosen time, the measured current is used to calculate $\mathbf{B}$ at each probe and the recorded voltage is integrated to find $\mathbf{V}_{int}$ at each probe. This leads to three matrix equations of the form $C\ \mathbf{V}_{int} = \mathbf{B}$ for each probe. These three equations are equivalent to the single matrix equation

$$C\ V_{int} = B \tag{8.3}$$

where the ith column of V_{int} is the vector $\mathbf{V}_{int}$ from a specific calibration shot and the ith column of B is $\mathbf{B}$ from the same calibration shot. We can solve for C to yield

$$C = B\ V_{int}^{-1} \tag{8.4}$$

By this procedure, we can calculate the calibration matrix C for each probe. The calibration matrices are then used to calculate the magnetic field at each probe location over the course of a plasma shot using $C\ \mathbf{V}_{int} = \mathbf{B}$.

8.2 Additional Corrections to Magnetic Field Measurements

Aside from using the a calibration matrix to calculate $\mathbf{B}$ from the measured voltages, there are two additional corrections that must be made to the magnetic field data in order to ensure its accuracy. The first correction is a simple offset removal on the measured voltages. Before integrating V to get V_{int}, the average voltage during the first 3 μs of data collection on each channel is subtracted from all measured voltages on said channel. This is because each channel of the digitizer using to measure the voltage on each magnetic pickup coil has a unique offset due to imperfect zeroing. While this offset is usually small, it's affect on V_{int} is large, especially later in the shot because the integral of a small constant is a straight line.

An additional error in the magnetic field measurements occurs due to capacitive coupling between the probes and plasma. The voltage recorded on any given coil is the sum of the inductive voltage and capacitive voltage, $V = V_{ind} + V_{cap}$. The capacitive voltage occurs as a result of a net charge momentarily appearing in the plasma near the probe during a shot. The net charge creates an electric field on the probe which changes its voltage.

We observe that a calculation of the magnetic field which accounts for the digitizer offset leads to a magnetic field trace which levels out to a constant at about 100 μs. Plasma merging is indicated by the presence of changing magnetic field signals on the B-dot probe array which means that the plasma merging process is complete at around 100 μs into a shot. Since there cannot be a magnetic field after the plasma is gone, we conclude that a capacitive voltage which was on the probe while the plasma was present must have been integrated to yield the final constant. We do not know the full functional form of V_{cap}, so we model the false magnetic field caused by the capacitive voltage as a tanh function that begins at zero and ends at the value of the magnetic field after the plasma merging in over.

$$B_{false}(t) = \frac{B(110)}{2}\left(\tanh\left(\frac{1}{20}(t - 62.5)\right) + 1\right) \tag{8.5}$$

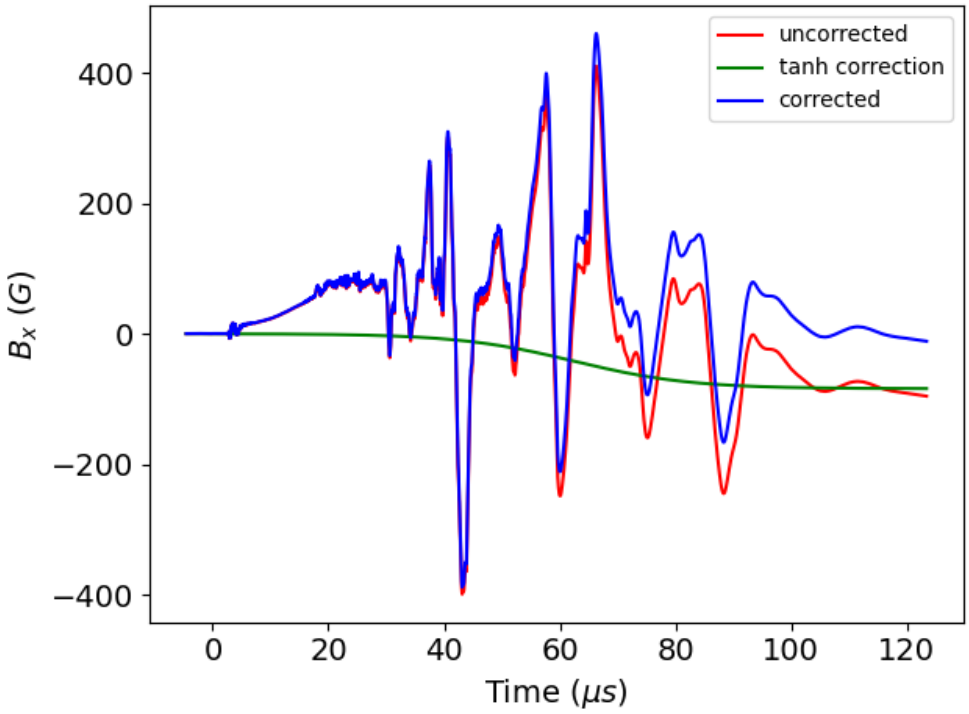

Figure 28: The x component of the magnetic field on probe 4 during shot 071323r51 with and without the correction for capacitive coupling. The tanh function that is subtracted from the uncorrected B_x in order to yield the corrected B_x is also shown.

This form of $B_{false}(t)$ reasonably approximates the capacitive voltage on the probe as a nonzero constant during the plasma merging and zero before and after the merging, because the derivative of $\tanh(t)$, $\text{sech}^2(t)$, is a smooth approximation of a rectangular pulse. $B_{false}(t)$ is subtracted from the magnetic field measurement to yield the true magnetic field as a function of time. Figure 28 shows the magnetic field before and after the correction for capacitive coupling between the probe and plasma.

9 Bibliography

[1] M. Landreman, Undergraduate Thesis, Swarthmore College, 2003.

[2] J. L. Burch, T. E. Moore, R.B. Torbert, and B. L. Giles, Space Sci Rev **199**, 5-21 (2016).

[3] E. N. Parker, J. Geophys. Res. **62**, 509 (1957).

[4] T. W. Kornack, P. K. Sollins, and M. R. Brown, Phys. Rev. E **58**, 36 (1998).

[5] M. Kuar and M. R. Brown, J. Plasma Phys. **84**, 905840614 (2018).

[6] P. M. Bellan, Fundamentals of Plasma Physics. (Cambridge University Press, Cambridge 2006).

[7] M. R. Brown, SSX Tutorials.

[8] A. Beresnyak and US Naval Research Laboratory Plasma Physics Division, NRL Plasma Formulary. (October 2023).

[9] D. J. Griffiths, Introduction to Electrodynamics, 4th ed. (Cambridge University Press, Cambridge, 2021).

[10] M. R. Brown, Phys. Plasmas. **6**, 1717 (1999).

[11] Y-H Liu, M. Hesse, F. Guo, W. Daughton, H. Li, P. A. Cassak, and M. A. Shay, Phys. Rev. Lett. **118**, 085101 (2017).

[12] L. Comisso and A. Bhattacharjee, J. Plasma Phys **82**, 595820601 (2016).

[13] S. C. Hsu, T. A. Carter, G. Fiksel, H. Ji, R. M. Kulsrud, and M. Yamada, Phys. Plasmas **8**, 1916-1928 (2001).

[14] J. B. Taylor, Phys. Rev. Lett. **33**, 1139 (1974).

[15] C. R. Geddes, T. W. Kornak, and M. R. Brown, Phys. Plasmas **5**, 1027 (1998).

[16] A. Bondeson, G. Marklin, Z. G. An, H. H. Chen, Y. C. Lee, and C. S. Liu, Phys. Fluids **24**, 1682 (1981).

[17] S. Chandrasekhar and P. C. Kendall, Astrophysical Journal 126, 457 (1957).

[18] R. L. Stenzel and W. Gekelman, Phys. Rev. Lett. **42**, 1055 (1979).

[19] R. L. Stenzel and W. Gekelman, J. Geophys. Res. **86**, 649 (1981).

[20] R.L. Stenzel and W. Gekelman, Physica D **12**, 133 (1984)

[21] M. Yamada, Y. Ono, A. Hayakawa, M. Katsurai, and F. W. Perkins, Phys. Rev. Lett. **65**, 721 (1990).

[22] Y. Ono, M. Yamada, Phys. Rev. Lett. **76**, 3328 (1996).

[23] M. Yamada, H. Ji, S. Hsu, T. Carter, R. Kulsrud, Y. Ono, and F. Perkins, Phys. Rev. Lett. **78**, 3117 (1997).

[24] H. Ji, M. Yamada, S. Hsu, and R. Kulsrud, Phys. Rev. Lett. **80**, 3256 (1998).

[25] J. Shrock, Undergraduate Thesis, Swarthmore College, 2018.

[26] T. Gray, Undergraduate Thesis, Swarthmore College, 2001.

[27] C. D. Cothran, J. Fung, M. R. Brown, and M. J. Schaffer, Rev. Sci. Intrum. **77**, 063504 (2006).

[28] J. Fung, Undergraduate Thesis, Swarthmore College, 2006.

[29] M. R. Brown, K. D. Gelber, and M. Mebratu, Plasma **3**, 27-37, (2020).